

Assessing the Corrosion of Multi-Phase Mg-Al Alloys with High Al Content by Electrochemical Impedance, Mass Loss, Hydrogen Collection, and Inductively Coupled Plasma Optical Emission Spectrometry Solution Analysis

Leslie G. Bland,^{‡,*} L.C. Scully,^{*} and J.R. Scully^{*}

ABSTRACT

The corrosion behavior for several die-cast Mg-Al alloys (AM50, AM60, and AZ91) was compared to commercial purity Mg and AZ31B-H24 utilizing simultaneous measurement of electrochemical impedance spectroscopy (EIS), hydrogen gas collection over a 24 h immersion period, gravimetric mass loss, and inductively coupled plasma optical emission spectrometry (ICP-OES) solution analysis of the total Mg concentration released. Tests were conducted in three electrolytes, unbuffered 0.6 M NaCl, 0.1 M tris(hydroxymethyl)amino-methane (TRIS), and 0.6 M NaCl buffered with TRIS to a pH of 7. EIS derived polarization resistance was monitored periodically, as determined from EIS circuit modeling using data collected to 0.001 Hz, and considering the pseudo-inductive low-frequency impedance time constant. EIS derived corrosion rates and oxidation charge density were similar to charge density determined from cumulative mass loss, ICP-OES solution analysis, and the volume of hydrogen collected for the die-cast AM50, AM60, and AZ91, as well as for Mg and AZ31B determined previously. The variation in the cathodic hydrogen evolution reaction kinetics for the die-cast alloys were also determined over 0, 3, 12, and 24 h immersion periods and compared to commercial purity Mg and AZ31B-H24. The global corrosion rate decreased with increasing Al content, even though Al wt% above the solubility limit (2 wt% at room temperature) resulted in increasing volume fractions of the $Al_8Mn_5(Fe)$, Al_2Mn_3 , and Al_3Fe intermetallic particles. Each of

the alloys contained varying volume fractions of primary α , β -phase ($Mg_{17}Al_{12}$), and eutectic $\alpha+\beta$ depending on Al content and processing. Al in the solid solution α -Mg phase decreased the overall net anodic reaction rate for the Mg^{2+} half-cell reaction. The $Mg_{17}Al_{12}$ phase was reasoned to not function as a strong cathode as deduced from cathodic E-log(i) studies. Moreover, the extent of anodically-induced cathodic activation was speculated to decrease with increasing Al content, which was a factor in determining overall corrosion rate and accumulated damage. However, corrosion damage depth as determined from a pitting factor analysis increased with Al content.

KEY WORDS: corrosion rate, electrochemical impedance spectroscopy, hydrogen evolution, inductively coupled plasma optical emission spectrometry, magnesium, monitoring, pitting factor, polarization, Tafel extrapolation

INTRODUCTION

Die-Cast Alloys and Metallurgy

Die-cast Mg-Al alloys are typically used as automotive parts such as seat frames, steering wheels, and safety parts because of their light weight, good castability, and good mechanical properties at room temperature.¹ Therefore, casting is a predominant processing route for Mg components² because of their good fluidity and low susceptibility to hydrogen porosity.³ During die-casting, the material is melted and resolidified, which leads to large variations in the distribution of solute elements, the formation of intermetallic particles (IMPs), and a randomized crystallographic texture.⁴ During resolidification, the solute elements are more soluble in the liquid state than the solid state; therefore, regions that solidify last are enriched in solute. These

Submitted for publication: October 19, 2016. Revised and accepted: January 17, 2017. Preprint available online: January 17, 2017, <http://dx.doi.org/10.5006/2308>.

[‡] Corresponding author. E-mail: lgb4df@virginia.edu.

^{*} Department of Materials Science and Engineering, University of Virginia, Charlottesville, VA 22904.

^{**} Fontana Corrosion Center, Department of Materials Science and Engineering, The Ohio State University, Columbus, OH 43210.

solidification boundaries and IMPs, which form during processing⁵⁻⁹ have unique electrochemical characteristics and can function as active cathodes during corrosion.^{6,10-11}

The resultant microstructure of Mg-Al, die-cast alloys is well known.¹²⁻¹⁹ The microstructure of these alloys, containing above 3 wt% Al, contain some amount of the β -phase ($\text{Mg}_{17}\text{Al}_{12}$) as well as other Al-Mn and Al-Mn-Fe IMPs.¹² According to the lever rule on an equilibrium Mg-Al phase diagram given a fixed Al content equal to the overall level, the mass% of AZ31 (UNS M11311⁽¹⁾) phases would consist of 97 wt% α -Mg and 3 wt% β -phase, AM50 (UNS M10501) would consist of 93 wt% α -Mg and 7 wt% β -phase, AM60 (UNS M10601) would consist of 90 wt% α -Mg and 10 wt% β -phase, while AZ91 (UNS M11916) would consist of 83 wt% α -Mg and 17 wt% β -phase. However, this estimation is not accurate for die-casting. During non-equilibrium casting, varying amounts of this phase are formed, with increasing amounts of the β -phase formed (but below the equilibrium limit) with increasing Al concentration (i.e., 5 wt% in AM50 < 6 wt% in AM60 < 9 wt% in AZ91).¹² However, a much lower volume fraction of β -phase is often produced than predicted by the lever rule under equilibrium assumptions.¹² The amount and distribution of these phases is highly dependent on the composition of the Mg-Al alloy as well as the processing parameters.^{7,17-26} AM50, AM60, and AZ91 studied herein were all processed using die casting and therefore the focus of the discussion is on the overall composition of the alloy.

Despite the additional added Al to the alloy, the Al concentration in solid solution in the primary α -Mg would be theoretically similar for AZ31B, AM50, AM60, and AZ91D under equilibrium conditions. The Al content is determined by the solvus line between Mg solid solution and $\text{Mg}_{17}\text{Al}_{12}$ for temperatures close to room temperature defining the highest equilibrium concentration of Al in solid solution without precipitating additional $\text{Mg}_{17}\text{Al}_{12}$ within the primary α -Mg as a secondary phase.²⁷ In contrast, the amount of divorced eutectic may vary and hence the amount of β -phase ($\text{Mg}_{17}\text{Al}_{12}$) likely differs based on Al, Zn, and Mn content and processing. Moreover, the non-equilibrium conditions during processing may result in differing Al contents in eutectic α -Mg compared to primary α -Mg.^{19,28-29} Crystal orientations may differ as well. These alloys contain Mn additions which are designed to getter Fe. However, the Mn also partitions some of the Al into Al-Mn and Al-Mn-Fe IMPs. For the low Al-content alloys such as AZ31 (i.e., ≤ 3 wt% Al), the remainder of the Al is in solid solution in the α -Mg phase. However, in AM50, AM60, and AZ91, the additional Al that is not in the form of Al-Mn series of

intermetallics and quenched into the alpha solid solution contributes to formation of β -phase. The Zn, present in AZ91, is retained in both the α -matrix as well as in the β -phase as it is soluble in both.²⁷

Corrosion of Al-Containing Alloys

The corrosion rate of Mg-Al alloys, with varying Al content, has been studied in many contexts.^{1,7,13,15-17,19,30-33} In particular, the corrosion rate of Mg-Al alloys in relationship to the amount of β -phase present in the alloy has been considered.^{7,17,19} Similarly, a large amount of literature details the atmospheric corrosion of these high Al-content Mg alloys.^{1,13,15-16,30-33}

While Mg-Al alloys are known for their low weight, this family of alloys are highly reactive because of their low electrochemical potential in the galvanic series and the existence of a microgalvanic couple between α -Mg grains of varying Al contents, the Al-Mn series of intermetallics, and β -phase ($\text{Mg}_{17}\text{Al}_{12}$).³⁴⁻³⁵ These alloys are particularly susceptible to microgalvanic corrosion as a result of the Al-rich cathodic secondary phases present in the material.^{6,10} The effect of the β -phase has two opposing effects on the corrosion behavior: (1) the β -phase can function as a galvanic alloy, coupled locally as a cathode during corrosion initiation because of its >150 mV, depending on exact solution, more positive open-circuit potential (OCP) ($\sim 1.3 V_{\text{SCE}}$), and therefore increase the corrosion rate of Mg-Al alloys; and (2) the β -phase can function as a *lateral* corrosion barrier.^{18,36-37} β -phase can form stable oxide films because of the presence of Al, stable as $\text{Al}(\text{OH})_3$ (at low to near-neutral pH) or Mg at a high pH, stable as $\text{Mg}(\text{OH})_2$ (according to independent consideration of their respective Pourbaix diagrams³⁸). Microgalvanic coupling between the primary α -Mg and β -phase can still occur, but the oxides may regulate cathodic reaction rates especially as Al enrichment occurs.²⁸⁻³⁰ The variation in this corrosion response is also highly dependent on the amount and distribution of this phase within the alloy where the fraction of this phase can be altered through different processing techniques as well as other alloying elements.^{7,17-26} However, the conditions governing β -phase behavior as either a cathode or as a barrier are unclear. Better understanding on the effects of β -phase, Al, Mn, and Zn are important to understand the overall corrosion behavior of Mg-Al and Mg-Al-Zn alloys. Variations in experimental design such as electrolyte chemistry, solution pH, and immersion time can significantly alter corrosion rates.³⁹ Moreover, differences in the corrosion rates occur based on short-term versus long-term estimation methods.⁴⁰⁻⁴¹ The instantaneous corrosion rate has been called into question, especially when determined by Tafel extrapolation from polarization curves, H_2 evolution rate, electrochemical impedance spectroscopy (EIS) derived charge transfer resistance, R_{CT} ,⁴² and spectrochemical approaches

⁽¹⁾ UNS numbers are listed in *Metals and Alloys in the Unified Numbering System*, published by the Society of Automotive Engineers (SAE International) and cosponsored by ASTM International.

TABLE 1
Compositions of 99.9% Mg Rod and Various Mg-Al Alloys^(A)

	UNS #	Al	Mn	Zn	Si	Cu	Ni	Fe	Mg
Mg Rod	—	0.01	0.01	0.01	0.021	0.005	0.001	0.006	Bal.
AZ31B-H24	M11311	3.02	0.33	0.99	0.025	0.005	0.002	0.005	Bal.
AM50A	M10501	5.0	0.5	0.22	<0.10	0.01	0.002	0.004	Bal.
AM60B	M10601	6.0	0.5	0.22	<0.10	0.01	0.002	0.005	Bal.
AZ91D	M11916	9.3	0.15	0.99	<0.30	0.01	0.002	0.005	Bal.

^(A) All compositions reported in wt%, with the actual compositions provided by QUANT (Quality Analysis and Testing Corporation).

conducted over the short-term.⁴³⁻⁴⁴ However, long-term cumulative corrosion damage can be assessed by mass loss, measurement of the H₂ evolved over the full immersion time, solution analysis for Mg²⁺ cations, and integration of corrosion rate (*i*_{corr}) versus time data determined by the evolution of polarization resistance (*R*_p) over time when including inductance.⁴¹ Even comparing 3 h to 24 h immersion results for the same environment and alloy can lead to large variations in the resultant estimated overall corrosion rate as a result of variations in the galvanic couple behavior, electrolyte pH, and Mg(OH)₂ formation over these time periods because of changes with time^{41,45} and different microstructural features dominating the corrosion rate at different immersion times. However, only a few studies apply all of these methods to Mg-Al alloys, which have mainly been studied by damage assessment and galvanic coupling experiments.²⁸⁻³⁰

Objective

The objective of this study is to evaluate the corrosion of die-cast Mg-Al alloys containing solidification structures formed during a typical casting resolidification process. The work herein gives the first estimate of instantaneous corrosion rate for a broad range of Mg-Al alloys using a rigorous analysis based on four of these approaches over a 24 h time period to provide a better understanding of the electrochemical behavior of Mg-Al alloys with various Al content. In order to facilitate comparisons, commercial purity (CP) Mg and AZ31B-H24 were compared based on previous studies to examine an Al-free material and a broader range of Al contents.^{39-40,46}

EXPERIMENTAL PROCEDURES

Materials

Three as-die-cast Mg-Al alloys, supplied by US Magnesium LLC[†], AM50A (UNS M10501), AM60B (UNS M10601), and AZ91D (UNS M11916), were characterized for the variation in their corrosion rates with increasing Al content (compositions are listed in Table 1). The corrosion rates were compared to commercially pure (CP) Mg and AZ31B-H24.^{39-40,46}

[†] Trade name.

⁽²⁾ Z = atomic number correction, A = absorption correction, F = fluorescence correction.

The wrought surface was prepared by grinding in ethanol with silicon carbide paper to a final grit of 1200.

Metallurgical Characterization

All samples were examined along the SL surface, polished through colloidal silica and etched with a picric acid etch (3 g picric acid, 30 mL acetic acid, 100 mL ethanol, and 15 mL distilled water) to determine the grain size and microstructure. Samples were analyzed using scanning electron microscopy (SEM) on a FEI Quanta 650[†] microscope. Images were taken at a working distance of 10 mm and an accelerating voltage of 5 kV. Electron backscatter diffraction (EBSD) was obtained for each alloy at a working distance of 15 mm and an accelerating voltage of 20 kV. EBSD allowed for detection of the volume fraction of the primary α -Mg as well as various IMPs. Compositional analysis was performed using energy dispersive spectroscopy (EDS) methods with ZAF⁽²⁾ corrections on the Aztec[†] software tool.⁴⁷ Images were recorded at a working distance of 10 mm while operating at an accelerating voltage of 5 kV. The grain size was determined using the linear intercept method at both 5 \times and 20 \times magnification via ASTM Standard E113-96.⁴⁸ The corrosion morphology was examined for each alloy to determine how the corrosion initiated and progressed over 24 h. The sample was marked using a Vickers hardness tester to enable examination of the corrosion morphology, before and after exposure, at the same location. Secondary electron SEM micrographs were taken before immersion in 0.6 M NaCl and after immersion in 0.6 M NaCl for 24 h at OCP. All samples were cleaned with CrO₃ to remove any corrosion products and examine the corrosion morphology according to ASTM Standard G1.⁴⁹ The relative area fraction of primary α -Mg as well as the eutectic α + β and β -phase were determined through image analysis (using a combination of backscatter and secondary electron micrographs) using ImageJ[†].⁵⁰

The solutions for the EIS and H₂ collection were pre-saturated with H₂ which would cause the pH to increase before the test (as discussed below). However, the solution before exposure tests were not saturated to retain in the corrosion/active region of the Pourbaix diagram in order to achieve the worst case scenario to determine where corrosion initiates and propagates, in correlation to microstructural

characteristics on the sample surface. However, it is also noted that, even under short immersion times and as a result of the rapid alkalization of the sample surface (which has been observed in multiple tests by the authors of this manuscript as well as other works) the pH of the surface rapidly increases to a pH of ~11. Therefore, the effect of the starting pH (in an unbuffered hydrogen pre-charged solution) would be minimized.

Characterization of the Corrosion Behavior of Mg-Al Alloys

Anodic charge density produced (over 24 h) was determined under full immersion conditions with four parallel and simultaneous techniques: (1) EIS, (2) gravimetric mass loss, (3) H₂ gas collection, and (4) inductively coupled plasma optical emission spectroscopy (ICP-OES) solution analysis. All experiments were run at least three times and the most typical cases are shown herein. A vertical electrochemical test cell with a Pt counter electrode and a saturated calomel electrode (SCE) was used which allowed for collection of H₂ into a vertical funnel and burette.³⁹⁻⁴⁰ All EIS scans were acquired from 100 kHz to 0.001 Hz with 6 points per decade and an AC amplitude of ±20 mV. EIS spectra were fit using ZView† to an equivalent circuit previously established and shown in Figure 1.^{39-40,51}

The equivalent circuit shown in Figure 1 consists of three time constants. R_s in the circuit represents the solution resistance and is specific to the exposure environment. R₁ and R₃ represent the resistances resulting from anodic and cathodic reactions on the sample surface which affect the local environment. The capacitors, C₁ and C₂, represent charge separation at the sample surface from the oxide/hydroxide layers and a combined adsorption type pseudo capacitance similar to a double layer capacitance. R₂ is the charge transfer resistance (the sum of R₁ and R₂ is often called R_{CT} in other work).^{11,40,51} Last, the inductor L₁ is taken to represent relaxation of the coverage of adsorbed intermediates in corroding areas of the sample surface but might also represent more complex effects such as darkening during corrosion.⁵²⁻⁵³

Before electrochemical testing, the electrolyte was pre-saturated with H₂ as it has been shown that H₂ gas is extremely soluble in aqueous environments.⁵⁴ Tests were performed in unbuffered 0.6 M NaCl (starting pH ~5.3 before it was pre-saturated with H₂ and measuring ~10 after pre-saturation) at OCP. The pH was monitored and typically rose to ~10 in 24 h regardless. Following testing, samples were cleaned according to ASTM G1 using 200 g/L CrO₃ and left to dry in a dry box for 24 h.⁴⁹

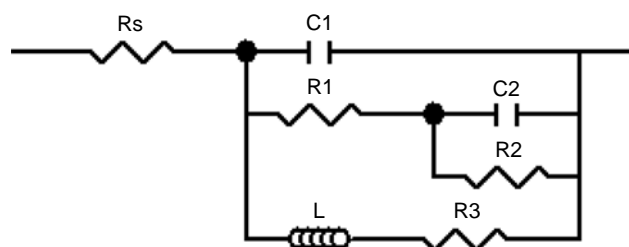


FIGURE 1. Equivalent circuit diagram used to model pseudo-inductive electrochemical impedance response associated with two RC time constants and inductive time constant associated with adsorbed intermediate coverage relaxation on corroding Mg in 0.6 M NaCl.

Corrosion rate was estimated using the Stern-Geary relationship:^{42,55}

$$i_{\text{corr}} = \frac{|\beta_a \beta_c|}{2.303 R_p (|\beta_a| + |\beta_c|)} \quad (1)$$

where β_a and β_c are the anodic and cathodic Tafel slopes, respectively, and $B = (1/2.303) \times |\beta_a \times \beta_c| / (|\beta_a| + |\beta_c|)$. Three different Tafel assumptions were used which were consistent with literature.^{39,56-57} Corrosion rate (i_{corr}) was converted to the anodic charge density produced (where $i_a = i_c$ at open circuit) over the full 24 h immersion test by integrating the EIS-estimated corrosion rate:

$$Q_a^{\text{EIS}} = \int \frac{|\beta_a \beta_c|}{2.303 R_p(t) (|\beta_a| + |\beta_c|)} dt \quad (2)$$

The mass loss of Mg ($\Delta m/\text{cm}^2$) or mass loss density was measured gravimetrically to ±0.1 mg resolution and converted to the anodic charge density (Q_a) via Faraday's law:³⁴

$$Q_a^{\Delta m} = z n F = \frac{z \Delta m F}{a} \quad (3)$$

where z is equivalent electrons per mole of Mg²⁺ oxidized, n is the number of moles of Mg, F is Faraday's constant (96,485 C/eq), and a is the molar mass of Mg. For each of the Mg-Al alloys, their equivalent weight was used to account for each of the given major alloying elements and their respective concentrations³⁴ as specified by ASTM G106.⁵⁸ This was determined as the sum the fractional number of equivalents of all alloying elements to determine the total number of equivalents in the alloy, N_{eq} :

$$N_{\text{eq}} = \sum \left(\frac{f_i}{a_i/z_i} \right) = \sum \left(\frac{f_i z_i}{a_i} \right) \quad (4)$$

The equivalent weight (g/eq) is then the reciprocal of the total number of equivalents ($\text{EW} = N_{\text{eq}}^{-1}$). The equivalent weight for AM50A, AM60B, and AZ91D were 11.99 g/eq, 11.95 g/eq, and 12.11 g/eq, respectively. This was determined assuming congruent Mg²⁺, Al³⁺, Mn²⁺, and Zn²⁺ oxidation⁽³⁾ which are justified

⁽³⁾ At a pH of ~11, Al dissolution occurs to Al(OH)₃ or AlO₂⁻ and Zn dissolution to ZnO or ZnO₂²⁻ are thermodynamically possible at the typical OCP and anodic polarization range of this study.

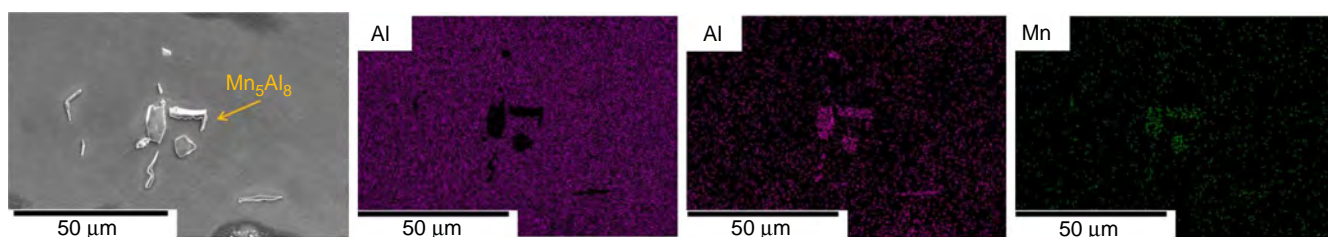


FIGURE 2. Typical secondary phase, Mn_5Al_8 , seen in the Mg-Al alloy system as shown in AM50.

given the thermodynamic properties of each element relative to the OCP of the Mg alloys and the assumption of the rise in pH to approximately 11.

The volume of H_2 gas evolved was converted to a corresponding cathodic charge density (Q_c) where $Q_a = Q_c$ at OCP³⁴ via Faraday's law and the ideal gas law. Thus:

$$Q_c^{H_2} = Q_a^{H_2} = znF = \frac{zPVF}{RT} \quad (5)$$

P is the pressure inside the burette (assumed to be approximately 1 atm [101.325 kPa] at sea level), V is the volume of H_2 gas collected, R is the ideal gas constant, and T is the temperature.

All solutions were analyzed using a Thermo Scientific iCAP 7200[†] ICP-OES. Samples were prepared by mixing 1 M HCl into the solution after electrochemical testing and sonicated to ensure that no undissolved corrosion product was left on the bottom of the container. The following wavelengths were used and recorded for the calculation of the charge produced for solution analysis: Mg (279.553 nm), Mg (280.270 nm), Al (226.910 nm), Al (308.215 nm), Al (396.152 nm), Fe (238.204 nm), Fe (239.562 nm), Mn (257.610 nm), Mn (259.373 nm), Zn (206.200 nm), and Zn (213.856 nm) following from previous work,⁴³⁻⁴⁴ where the detection limits for each of these elements have been reported elsewhere.⁵⁹ The ICP reports the concentration of elements in the collected solution (ppm), which can be similarly converted to anodic charge (Q_a^{ICP}) using Faraday's law [Equation [3)].

The average corrosion penetration depth ($x_{average}$) was calculated from Faraday's law:

$$x_{average} = \frac{Q(E.W.)}{F\rho} \quad (6)$$

where E.W. is the equivalent weight of commercially pure Mg, taken as 12.16 g/eq, F is Faraday's constant (96,485 C/eq), and ρ is the density of Mg. From this,

the degree of localized corrosion was determined from a localization factor (LF):

$$LF = \frac{x_{max}}{x_{average}} \quad (7)$$

The x_{max} was determined from 3D imaging using an Optical Hirox[†] microscope. These numbers have been reported as the average for ~5 measurements. The relative area fraction of primary α -Mg corroded was determined through ImageJ[†].⁵⁰

Anodic and cathodic kinetics were determined in unbuffered 0.6 M NaCl (pH ~5.3 and not saturated with H_2 to watch how the pH varied with time), 0.1 M buffered tris(hydroxymethyl)aminomethane (TRIS) (pH ~7), and 0.6 M NaCl buffered to a pH ~7 with TRIS. Samples were held at OCP for 0, 3, 12, and 24 h, respectively, followed a potentiodynamic polarization test. Cathodic potentiodynamic polarization scans ranged from 50 mV above OCP to -2.3 V below OCP in a downward sweep at a rate of 1 mV/s. Anodic potentiodynamic polarization scans ranged from 50 mV below OCP to 1.5 V above OCP in an upward sweep at a rate of 1 mV/s.

RESULTS

Cast Mg Alloy Metallurgical Characterization

The Al composition of the primary α -Mg matrix for the die-cast alloys (i.e., the amount of Al in solid solution) for each alloy is approximately the same (~2 wt%), as determined through quantitative EDS methods.¹² The additional Al content led to the formation of several Al-containing intermetallic particles (IMPs).^{6,18,46} EDS of each of the die-cast Mg-Al alloys indicated several secondary phases. An Al-Mn phase, likely Al_8Mn_5 , was seen in all three of the die-cast alloys (Figure 2), along the Mg-Al phase, $Mg_{17}(Al,Zn)_{12}$ (Figure 3). The Al_8Mn_5 appears as either cube-like or rod-like particles heterogeneously throughout the material. Similarly, two distinct morphologies were observed for the β -phase: (1) a pro-eutectic β -phase and (2) a eutectic, rod-like often directionally solidified and sometimes lamellar β -phase^{(4),6,18,46} (Figure 3). These structures are present to varying degrees in all three of these alloys. The example shown here was taken from the AZ91 sample to show the additional distribution of Zn in the β -phase. However, the morphology of

⁽⁴⁾ The cast structure in these alloys often solidifies first by primary α -Mg solid dendrite formation accompanied by the development of Al-enriched interdendritic liquid regions. These liquid regions later form β -phase and the remaining Al-depleted liquid solidifies as secondary or tertiary α -Mg. These structures are often referred to as "divorced eutectics" because the α and β phases are not formed cooperatively as in a normal lamellar eutectic growth, but are formed in separate decoupled steps.

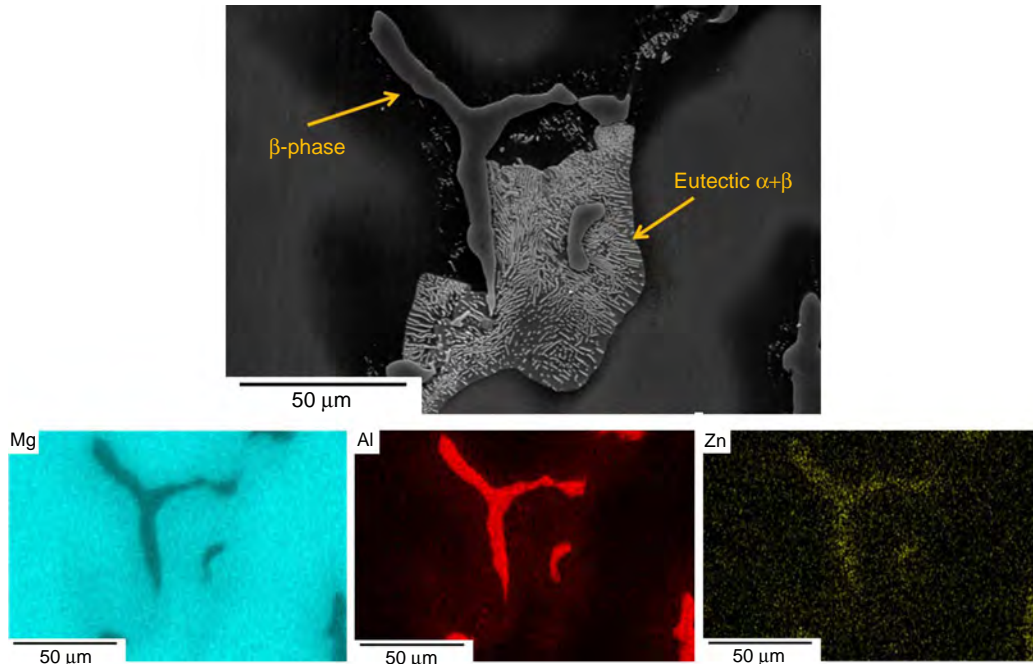


FIGURE 3. Typical secondary β -phase, $Mg_{17}(Al,Zn)_{12}$, and the eutectic secondary phase, seen in the Mg-Al alloy system as shown from AZ91.

this phase is similar for AM50 and AM60 (albeit without the additional Zn content).

The size and distribution of these phases was highly dependent on the specific alloy with the β -phase appearing as $Mg_{17}Al_{12}$ in AM50 and AM50 and $Mg_{17}(Al,Zn)_{12}$ in AZ91. Also, the morphology of this phase varied with Al content where this phase either appeared as the singular isolated β -phase or contained in a $\alpha+\beta$ eutectic. In the AM50 alloy, these β -phase and $\alpha+\beta$ eutectic structures were spaced approximately 50 μm apart with the Al-Mn and/or Al-Mn-Fe IMPs heterogeneously throughout the material (Figure 4[a]). Also, the EBSD of the AM50 revealed a randomized texture with relatively large grains ($\sim 500 \mu m$) (Figure 4[b]). As determined through EBSD phase identification, only a small phase fraction of the

microstructure was the β -phase while the Mn_5Al_8 phase was prevalent (Tables 2 and 3). The β -phase for this alloy was mainly contained in an $\alpha+\beta$ eutectic (Figure 5). This corresponded with image analysis of the area fraction of this eutectic phase which showed that, relative to the primary α -Mg, there was only a small area fraction of this eutectic phase, as indicated in Table 3.

In the AM60 alloy, these β -phase and $\alpha+\beta$ eutectic structures were spaced $\sim 25 \mu m$ and contained various Al-Mn and Al-Mn-Fe IMPs (Figure 6[a]). EBSD indicated no preferential texture (Figure 6[b]) and a grain size of $\sim 500 \mu m$. The β -phase was heterogeneously distributed throughout the material as well as several other IMPs, as determined through EBSD (Table 2). The β -phase consisted of both isolated β -phase as well

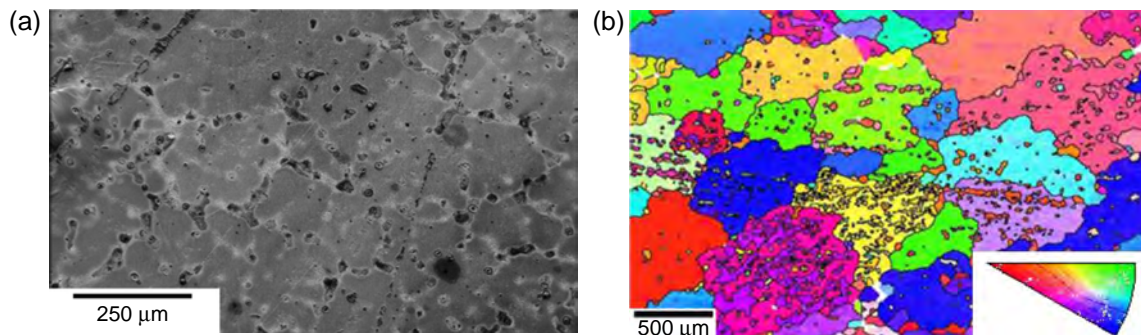


FIGURE 4. (a) Secondary SEM image of AM50 cast alloy with (b) corresponding EBSD.

TABLE 2

Phase Fraction of Various IMPs in Mg-Al Alloys, as Determined Through EBSD and Image Analysis^(A)

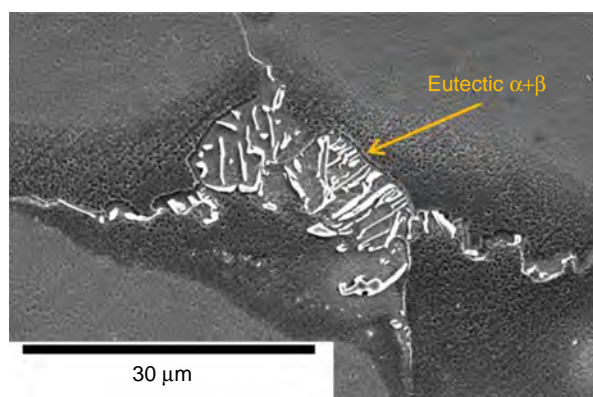
	Phase Fraction of α -Mg	Phase Fraction of β -Mg ₁₇ (Al,Zn) ₁₂	Phase Fraction of Al ₃ Mn ₂	Phase Fraction of AlFe ₃	Phase Fraction of Al ₈ Mn ₅
Mg Rod	1	—	—	—	—
AZ31B-H24	0.75	—	0.1	—	0.15
AM50A	0.61	0.10	0.12	0.01	0.16
AM60B	0.36	0.20	0.22	0.02	0.20
AZ91D	0.28	0.50	0.05	0.03	0.14

^(A) The remainder is primary α -Mg.

TABLE 3

Area Fraction of β -Phase and Eutectic $\alpha+\beta$ Relative to Primary α -Mg as Determined Through Image Analysis⁵⁰

	Area Fraction of β -Mg ₁₇ Al ₁₂	Area Fraction of Eutectic $\alpha+\beta$	Area Fraction of Primary α
AM50A	1	9	90
AM60B	10	10	80
AZ91D	20	5	75

FIGURE 5. Typical secondary β -phase, Mg₁₇Al₁₂, contained in a eutectic ($\alpha+\beta$), seen in the Mg-Al alloy system as shown from AM50.

as eutectic $\alpha+\beta$ (Figure 7, Table 3). However, it is noted that the β -phase contained outside of the eutectic is relatively small (in size) in comparison to AZ91.

The microstructure of the AZ91 alloy was also observed to consist of $\alpha+\beta$ eutectic as well as β -phase

(rich in Al-Zn because of the addition of Zn; Figures 3 and 8[a]). This alloy has the most closely spaced solidification structures ($\sim 15 \mu\text{m}$) with Al-Mn-Fe IMPs still distributed throughout the material (Figure 8[a]). EBSD of the material also had no distinct texture (Figure 8[b]). The AZ91 alloy contained the largest phase fraction of the β -phase but contained approximately the same phase fraction of other IMPs (Table 2). The AZ91 alloy had the highest amount of β -phase expressed as an area fraction distributed in the alloy as both an independent β -phase and as eutectic $\alpha+\beta$ (Figure 9, Table 3). Most of the β -phase present in this alloy was as the rod-like eutectic microstructure (Table 3).

In contrast, wrought AZ31B and CP Mg were used as a comparison. AZ31B wrought sheet is known to have a strong basal $\{0\ 0\ 1\}$ texture and contain Al₈(Mn,Fe)₅ but no β -phase, while extruded rod CP Mg is equiaxed with few impurities. The metallurgy of these materials is discussed elsewhere.^{10,59}

Resultant Corrosion Morphology of Al-Containing Cast Mg Alloy

Samples were immersed for 24 h at OCP in 0.6 M NaCl to observe the variation in the corrosion morphology with Al additions and phases formed. Comparative results in Mg and AZ31B under similar conditions are discussed elsewhere.⁵⁹ Samples were marked with a fiducial mark and imaged before corrosion. Corrosion was not seen to initiate until approximately 3 h to 4 h of immersion according to time-lapse videos (not shown for brevity). Compositional

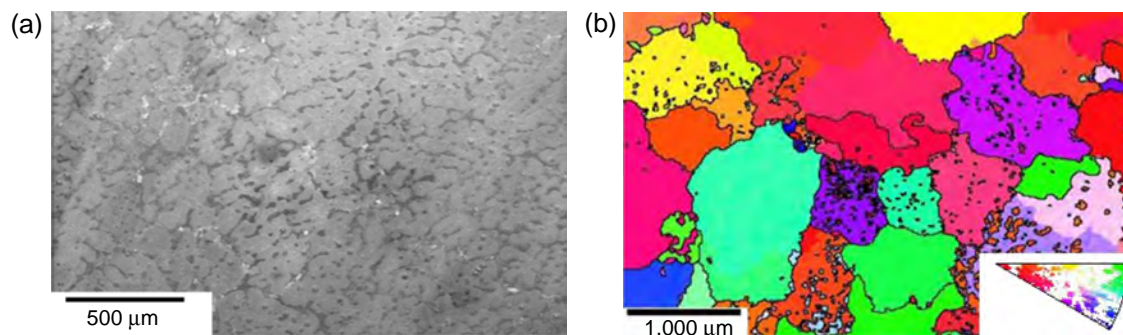


FIGURE 6. (a) Secondary SEM image of AM60 cast alloy with (b) EBSD.

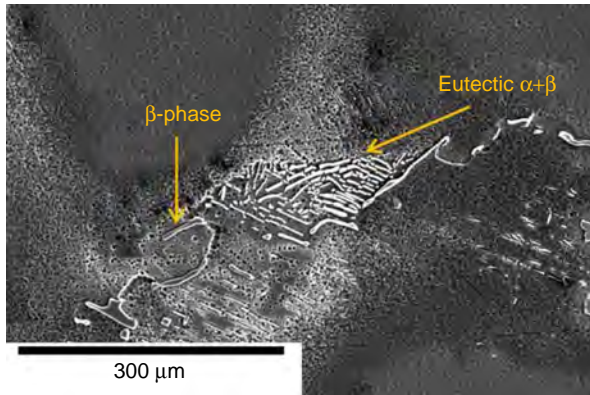


FIGURE 7. Typical secondary β -phase, $Mg_{17}Al_{12}$, contained in a eutectic ($\alpha+\beta$), as well as isolated β -phase, seen in the Mg-Al alloy system as shown from AM60.

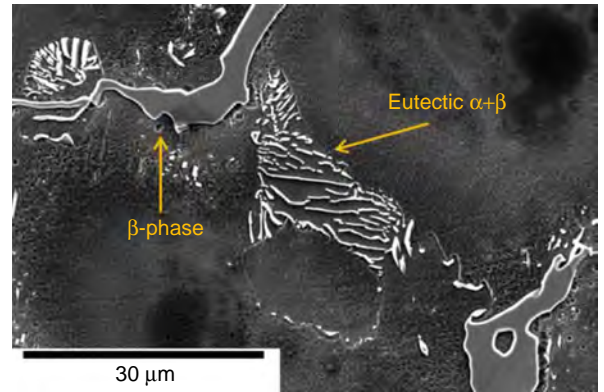


FIGURE 9. Typical secondary β -phase, $Mg_{17}Al_{12}$, contained in a eutectic ($\alpha+\beta$) as well as isolated β -phase, seen in the Mg-Al alloy system as shown from AZ91.

contrast on AM50 shows primary α , $\alpha+\beta$ eutectic, and the Al_8Mn_5 phase throughout the material, as confirmed through EDS analysis (Figure 10[a]). Corrosion initiated in selected primary α -Mg regions (Figure 10[b]). The exact Al content of the grain attacked was not known but often reported as lower than average or containing more Al-Mn IMPS.²⁸⁻³⁰ In AM60, the $\alpha+\beta$ eutectic as well as additional β -phase IMPs were observed throughout the material as well as the Al_8Mn_5 phase (Figure 11[a]). A large amount of the closely spaced β -phase is intact both before and after corrosion (Figures 11[a] and [b]). However, corrosion initiated in the primary α -Mg (Figure 11[b]). In some studies the primary α -phase was reported to have a lower Al content or contain less Al accumulation at interfaces but this was not verified here.²⁸⁻³⁰ In AZ91, the closely spaced divorced eutectic β -phase was observed throughout the sample (Figure 12[a]) and little corrosion occurred, even after 24 h of immersion at OCP (Figure 12[b]). Upon closer inspection, as shown in Figure 12(c), the β -phase was intact while the primary α -Mg matrix had corroded.

From image analysis of the relative amount of primary α -Mg corroded for each alloy, it was observed

that only a small area fraction of primary α -Mg was corroded on the sample surface (Table 3). Therefore, the corrosion was only in localized places on the sample surface. A LF was determined for each of the die-cast alloys and is discussed later to determine the variation in the corrosion on a local scale versus the global corrosion rate averaged over the entire surface area.

Corrosion Electrochemistry of Al-Containing Cast Mg Alloys in Comparison to AZ31B and CP Mg

Open-Circuit Potential with Time — The OCP was recorded as a function of time in 0.6 M NaCl for each Mg-Al alloy and compared to CP Mg and AZ31, as previously reported,^{40,59} after the samples were held at OCP for 0, 3, 12, and 24 h (Figure 13). The starting OCP for each alloy increased with time. The starting OCP for each alloy was approximately $-1.59 V_{SCE}$, which was slightly more positive than the OCP determined for AZ31, $-1.6 V_{SCE}$, and CP Mg had the most negative reported OCP ($-1.63 V_{SCE}$). Over the 24 h immersion period, the OCP increased for all alloys especially in the initial 3 h. During this time period, the pH of the solution had risen from ~ 5.3 to 7. However, from 3 h to 24 h of immersion time, it is noted that the AZ31 OCP

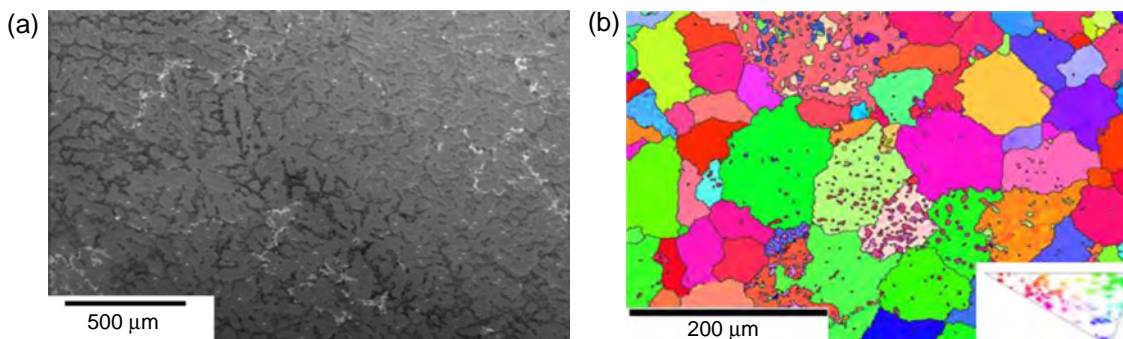


FIGURE 8. (a) Secondary SEM image of AZ91 cast alloy with (b) EBSD.

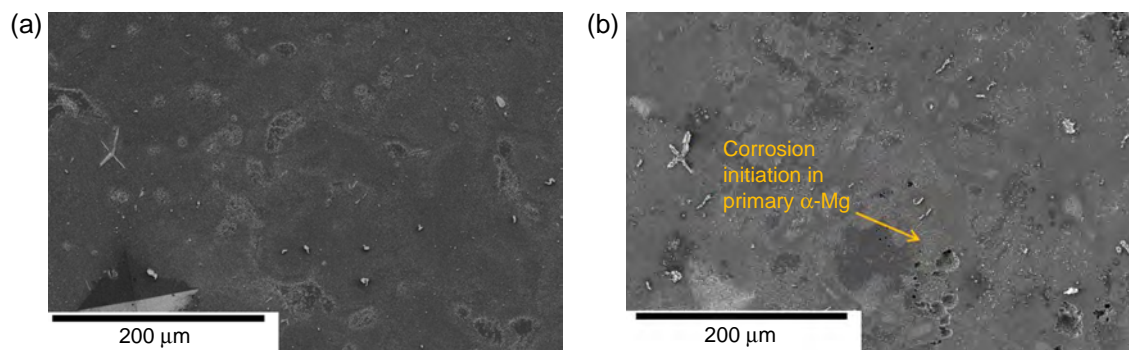


FIGURE 10. Secondary electron micrographs of (a) AM50 sample before exposure and (b) AM50 specimen after exposure and cleaned with CrO_3 to remove any oxides after 24 h immersion at OCP in 0.6 M NaCl.

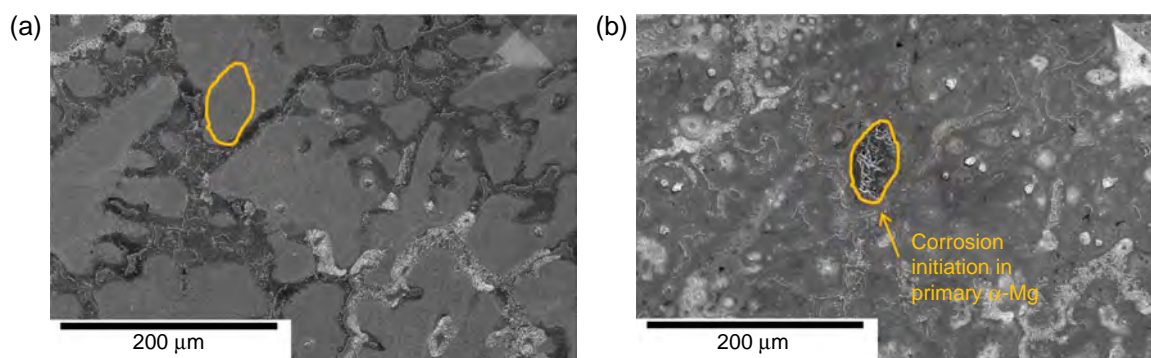


FIGURE 11. Secondary electron micrographs of (a) AM60 sample before exposure and (b) AM60 specimen after exposure and cleaned with CrO_3 to remove any oxides after 24 h immersion at OCP in 0.6 M NaCl.

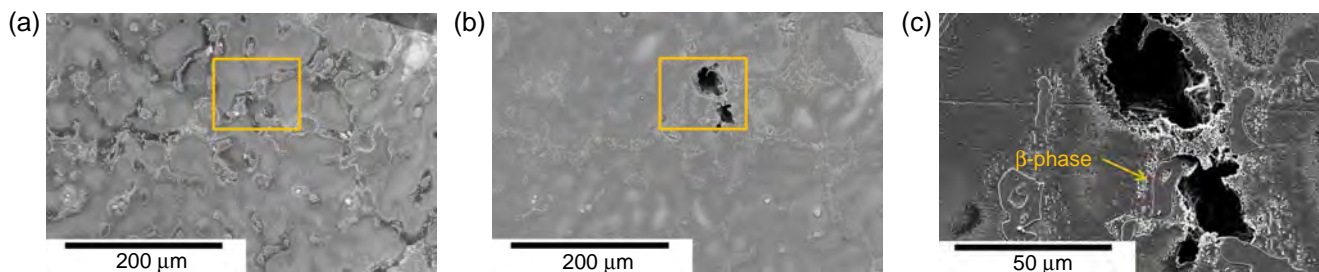


FIGURE 12. Secondary electron micrographs of (a) AZ91 sample before exposure, (b) AZ91 specimen after exposure, and (c) high-magnification micrograph of corrosion damage to the α -Mg matrix. The sample was cleaned with CrO_3 to remove any oxides after 24 h immersion at OCP in 0.6 M NaCl.

slightly increased, while the higher Al-content alloys (AM50, AM60, and AZ91), all retained approximately the same OCP measurements. After 3 h of immersion, the pH of the solution continued to increase to ~ 11 .

The OCP was also measured in two buffered neutral pH environments, 0.1 M TRIS and 0.6 M NaCl TRIS buffered with TRIS. The pH for these environments remained ~ 7 for the full exposure. In the 0.1 M TRIS environment, the measured OCP for each alloy was approximately $-1.5 V_{\text{SCE}}$. There was little variation with the OCP with alloy content. In 0.6 M NaCl buffered with TRIS, there was a slight increase in the

OCP from $-1.51 V_{\text{SCE}}$ to $-1.52 V_{\text{SCE}}$. However, the increase in this pH was much smaller than in unbuffered 0.6 M NaCl. There was a slight increase in the OCP with added Al content.

Corroborating Electrochemical Impedance Spectroscopy, Mass Loss, H_2 Collection, and Inductively Coupled Plasma Optical Emission Spectrometry of High Al-Containing Alloys After 24 Hour Corrosion at Open-Circuit Potential — The characteristic EIS response of Mg-Al alloys in chloride-containing environments shows the presence of two capacitive loops and an inductive loop which is similarly reported in CP Mg

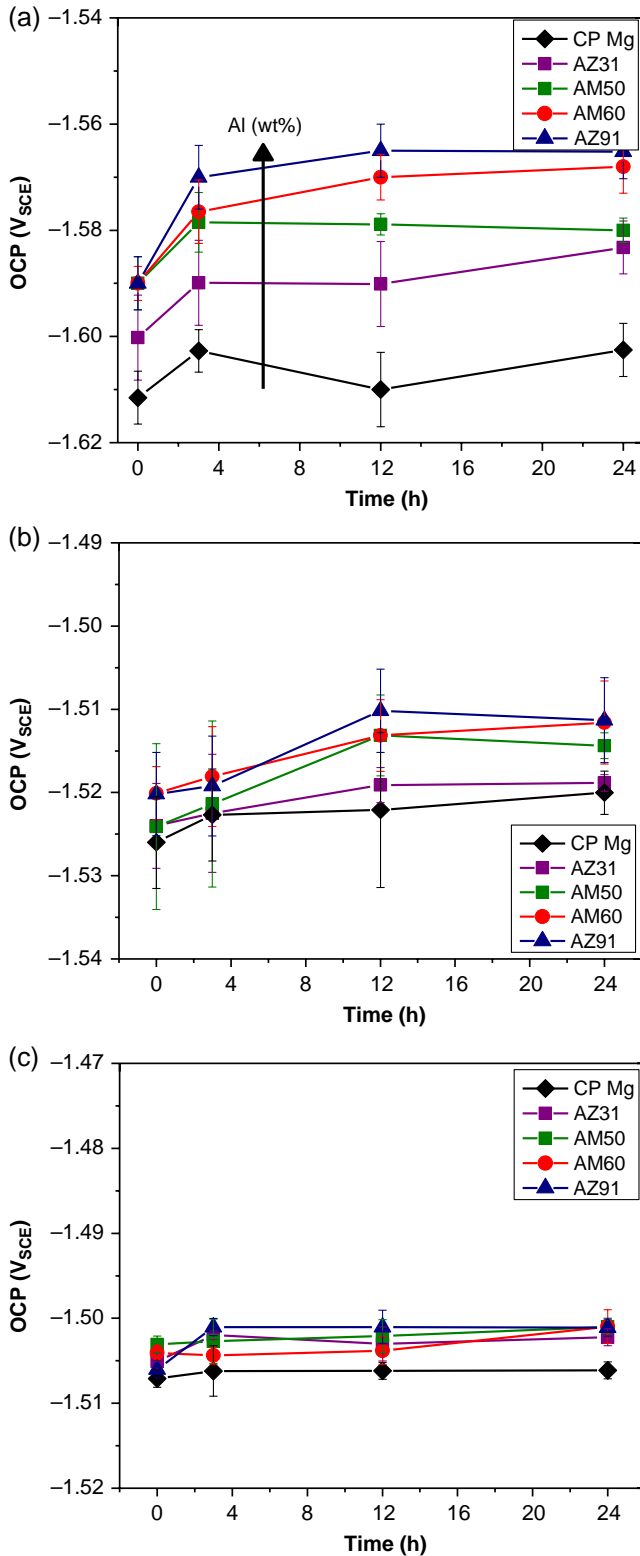


FIGURE 13. Measured OCP for CP Mg, AZ31, AM50, AM60, and AZ91 determined at 0, 3, 12, and 24 h in (a) 0.6 M NaCl, (b) 0.6 M NaCl buffered with TRIS to pH=7, and (c) 0.1 M TRIS.

⁽⁵⁾ Some previous work recognized the physical origin of these three time constants but did not use the EIS data at the low-frequency limit to determine the polarization resistance.

and AZ31B.^{14,52-53,60-65} Such behavior was also noted in Mg-Al alloys in sulfate.⁵²⁻⁵³ The use of a low-frequency inductor was required, as well as fitting to a significantly low enough frequency (~1 mHz) to acquire an accurate representation of corrosion rate including the relaxation of the adsorbed intermediate with potential (Figure 1).^{(5),66-68} The EIS behavior from each of the Al-containing Mg-Al alloys is shown in Figure 14 after 24 h of immersion in 0.6 M NaCl. A reasonably good fit was achieved for each of the die-cast alloys using the equivalent circuit shown (<15% error). Each of the fitting results is shown in Table 4. The R_p for each of the die-cast alloys was determined according to the respective equivalent circuit.

$$\frac{1}{R_p} = \frac{1}{R_1 + R_2} + \frac{1}{R_3} \quad (8)$$

From the EIS-determined R_p and i_{corr} , a notable increase in the R_p (a decrease in the i_{corr}) was observed with time in NaCl (Figure 15). This particularly occurs in the first 3 h after immersion in 0.6 M NaCl. The decrease in the corrosion rate with time is typically rationalized to occur as a result of the rapid alkalization of the Mg surface (as confirmed by the increase in the pH from ~5.3 to ~11 during the exposure time from tests where the pH was monitored under OCP conditions and the solution was not pre-saturated with H₂). In these studies it could also be a result of Al enrichment at the surface, although not confirmed here.²⁸⁻³⁰ The variation in the corrosion rate with time has been noted for other Mg alloys^{40,45} and is a rationale why comparing different immersion times and tests for Mg alloys can lead to large variations in observations and trends.

Integration of the corrosion current density over the 24 h immersion time using Equation (1), conversion of the mass loss using Faraday's law Equation (2), calculation of the H₂ collected over 24 h using the ideal gas law and Faraday's law, and measurement of the magnesium and other metal cations dissolved in acid solutions using ICP-OES and Faraday's law resulted in anodic charge estimations that were consistent with each other for a given alloy (Tables 5 and 6, Figure 16). Corrosion anodic charge varied with Al content. Several Tafel slope assumptions were utilized^{39,56-57} and it was shown that little variation in the EIS-determined corrosion rate was obtained, even with large variations in the Tafel assumptions. This is because Equation (1) is much more dependent on the EIS-determined R_p than reasonable variations in the Tafel slopes which produce small changes in B.⁴⁰ Further commentary is given below regarding the need for normalization by active corrosion area compared to wetted surface area.

Kinetics with Time— The anodic E-log(i) polarization kinetics for CP Mg, AZ31, AM50, AM60, and AZ91 were observed after 24 h at OCP (Figure 17[a]) for 0.6 M NaCl, 0.6 M NaCl buffered with TRIS, and 0.1 M TRIS,

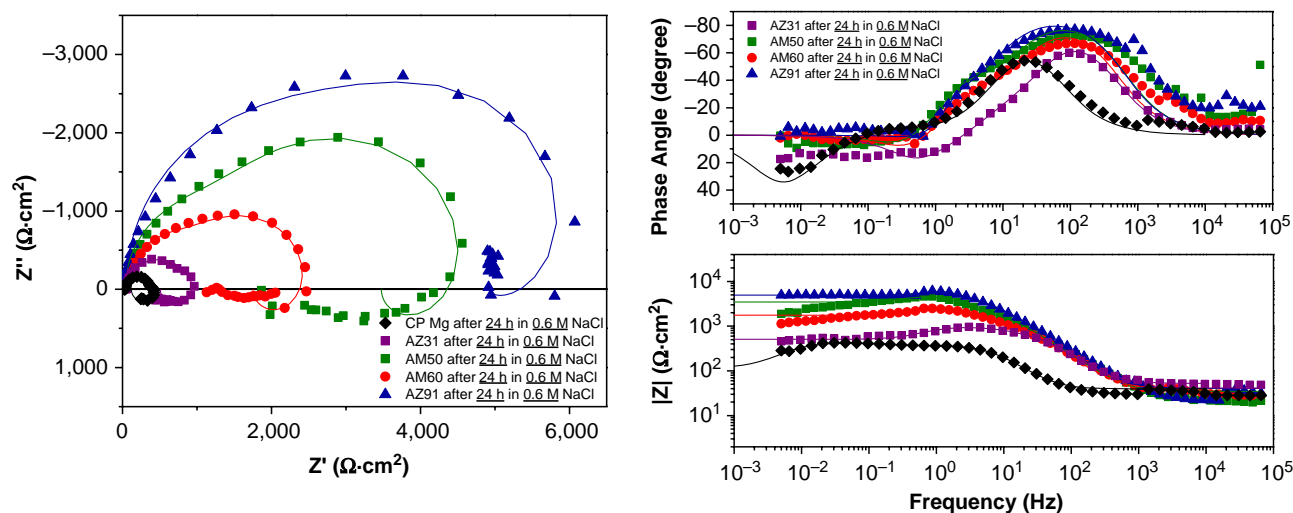


FIGURE 14. (left) Nyquist plots and (right) Bode magnitude and phase plot for CP Mg, AZ31B, AM50, AM60, and AZ91. Data shown along with respective fits following 24 h in 0.6 M NaCl at open circuit.

TABLE 4

Typical Fitting Results of Electrochemical Impedance Measurements Made on CP Mg, AZ31B, AM50A, AM60B, and AZ91D in 0.6 M NaCl at Open Circuit After 3, 12, and 24 Hours of Immersion^(A)

	CP Mg			AZ31B			AM50			AM60			AZ91		
	3 h	12 h	24 h	3 h	12 h	24 h	3 h	12 h	24 h	3 h	12 h	24 h	3 h	12 h	24 h
R_s ($\Omega\text{-cm}^2$)	81	93	100	32	31	31	19	27	26	30	33	41	23	43	41
C_1 ($\mu\text{F/cm}^2$)	160	110	90	19	21	24	7	6	7	8	8	8	5	6	6
R_1 ($\Omega\text{-cm}^2$)	140	390	820	690	440	600	1,870	2,550	1,092	1,130	1,460	1,390	2,220	4,670	4,630
C_2 ($\mu\text{F/cm}^2$)	3,600	9,500	4,700	40	70	48	2	12	31	69	44	45	20	30	18
R_2 ($\Omega\text{-cm}^2$)	22	77	160	310	180	300	2,360	3,880	1,050	792	1,490	1,190	1,670	7,000	6,500
L ($\Omega\text{-s-cm}^2$)	3,610	9,870	26,200	310	230	300	3,730	16,900	6,120	3,930	3,040	2,360	1,490	1,790	650
R_3 ($\Omega\text{-cm}^2$)	100	100	100	1,160	680	1,150	7,880	18,100	3,830	5,740	6,030	5,040	5,380	8,130	4,890
R_p ($\Omega\text{-cm}^2$)	62	83	91	470	170	320	2,750	4,740	1,370	1,440	1,980	1,710	2,260	4,790	3,400

^(A) As per the equivalent circuits seen in Figure 1. All runs were performed with a vertical flat cell with a 1 cm² sample window.

and typical anodic E-log(i) curves are shown. Little difference was observed for AM50, AM60, and AZ91 with respect to the anodic kinetics in each of these environments when comparing uncorrected data (Figure 17[a]). This agreed with previous work which showed that the kinetics of anodically driven Mg-Al alloys, where corrosion is forced to occur primarily in the primary α -Mg matrix, did not vary given the same solid solution Al composition in the primary α -Mg matrix.⁴⁶ However, the die-cast alloys (which have a slightly higher Al content) exhibited slightly reduced net anodic kinetics as a function of potential in the charge transfer control region in comparison to CP Mg and AZ31B (Figure 17[a]).

IR correction of i-E data was performed via the linear E-log(i) fit method in 0.6 M NaCl. R_Ω was determined to be $\sim 100 \Omega$ (1 cm² test area), as obtained from EIS (Table 4). From the IR corrected anodic potentiodynamic scans for the die-cast alloys, there is a low apparent anodic Tafel slope of about 25 mV/dec to 30 mV/dec that is representative of a non-polarizable charge transfer controlled Mg oxidation process on all alloys (Figure 17[b]).³⁹⁻⁴⁰ While these rapidly acquired anodic characteristics make it difficult to calculate accurate long-term corrosion rates using either Tafel extrapolation or linear polarization resistance based techniques, the IR corrected data can be used to make an assessment of the true anodic kinetics of the favorable primary α -Mg corrosion phase at a given time. Jones' approach was utilized to obtain a more accurate anodic rate but neglecting the negative difference effect, independent of i_c ($|i_a| = |i_{app}| + |i_c|$).³⁴ In Figure 17(b), it is shown that the corrected anodic dissolution kinetics decrease as a result of the addition of Al to the alloy.⁽⁶⁾ That is, higher Al content in AM

⁽⁶⁾ It is recognized that the correction is incomplete as a fixed i_c was utilized not correcting for the well-known negative difference effect. Moreover, it is also recognized that the anodic data included anodic polarization of the β -phase which contributes to i_a . However, this is believed to introduce less than 10% error resulting from the combined effect of the small area fraction and the lower anodic dissolution rate.

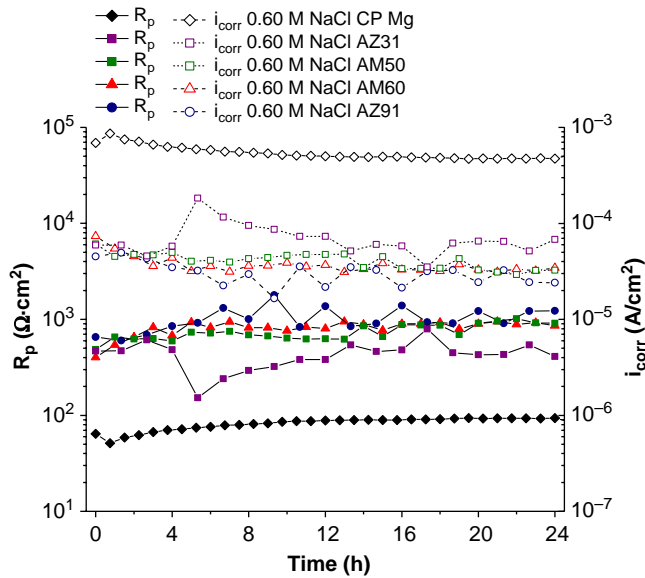


FIGURE 15. Typical EIS-estimated polarization resistance and corresponding corrosion current density (taking into account the total surface area) vs. time of exposure in 0.6 M NaCl on CP Mg, AZ31B, AM50, AM60, and AZ91.

alloys and AZ91 exhibit lower anodic reaction rates over a range of anodic potentials.

Typical cathodic polarization curves for CP Mg, AZ31, AM50, AM60, and AZ91 after 24 h at OCP are shown in Figure 18 for 0.6 M NaCl; 0.6 M NaCl buffered with TRIS and 0.1 M TRIS are excluded for brevity but showed no trends. In the 0.6 M NaCl environment, only a slight difference in the cathodic kinetics was shown with varied alloying content (Figure 18). After 3 h (Figure 18[a]), the cathodic kinetics did not vary with each alloy. However, after 24 h at OCP the cathodic reaction rate increased with increasing Al content. In contrast, little variation in the cathodic kinetics was shown for either the 0.6 M NaCl environment buffered with TRIS or 0.1 M TRIS. These data were also excluded for brevity.

DISCUSSION

Resultant Corrosion Morphology in High Al-Containing Cast Mg Alloys

From the resultant morphology (Figures 10 through 12), much less surface corrosion propagation of dark attack areas occurs in the die-cast Mg-Al alloys than in the previously studied AZ31.⁵⁹ In the literature, low Al-containing alpha grains are argued to be responsible for corrosion sites or those with fewer Al-Mn

TABLE 5
Anodic Charge Density Produced by Oxidation of CP Mg, AZ31B, AM50A, AM60B, and AZ91D^(A)

		Tafel Assumptions				
		CP Mg	AZ31B	AM50	AM60	AZ91
B_{King}^{41}	β_c (mV/dec)	315.0	315.0	315.0	315.0	315.0
	β_a (mV/dec)	112.5	112.5	112.5	112.5	112.5
	B (mV/dec)	36.0	36.0	36.0	36.0	36.0
	ΣQ_{EIS} (C/cm ²)	97.5±18.3	15.9±5.3	5.9±1.0	3.1±0.5	2.5±0.2
B_{Shi}	β_c (mV/dec)	160.0	160.0	160.0	160.0	160.0
	β_a (mV/dec)	180.0	180.0	180.0	180.0	180.0
	B (mV/dec)	36.8	36.8	36.8	36.8	36.8
	ΣQ_{EIS} (C/cm ²)	99.6±17.6	13.1±4.5	6.0±1.0	3.2±0.5	2.6±0.2
B_{Cao}	B (mV/dec)	31.1	31.1	31.1	31.1	31.1
	ΣQ_{EIS} (C/cm ²)	84.1±12.2	11.1±3.2	5.1±0.9	2.7±0.4	2.2±0.2

^(A) As calculated by integration of i_{corr} derived from EIS-estimated polarization resistance for three different Tafel approximations after exposure to unbuffered 0.6 M NaCl at open circuit for 24 h. Results are normalized to the exposed sample area.

TABLE 6
Anodic Charge Produced by CP Mg, AZ31B, AM50A, AM60B, and AZ91D^(A)

	CP Mg	AZ31B	AM50	AM60	AZ91
Δm (mg)	6.7±1.0	1.1±0.4	0.3±0.4	0.2±0.4	0.2±0.4
$\Sigma Q_{\Delta m}$ (C/cm ²)	104.9±20.6	16.9±5.7	7.98±0.2	6.86±3.9	5.78±2.1
ΔV_{H_2} (cm ³)	5.71±1.4	1.0±0.3	0.65±0.4	0.3±0.3	0.45±0.2
ΣQ_{H_2} (C/cm ²)	97.93±23.6	16.6±4.6	7.51±1.2	2.44±1.5	3.2±1.8
ΣQ_{ICP} (C/cm ²)	71.55±14.3	21.2±8.0	6.52±3.2	5.67±1.6	2.54±1.3

^(A) As calculated by mass loss, hydrogen accumulation, and ICP-OES after exposure in 0.6 M NaCl at open circuit for 24 h. Results are normalized to the sample area.

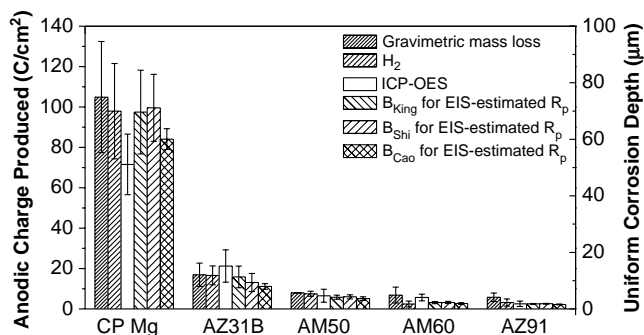


FIGURE 16. Anodic charge produced per total electrode area during corrosion of die-cast AM50, AM60, and AZ91 in comparison to wrought plate AZ31B-H24 and CP Mg in 0.6 M NaCl at open circuit after 24 h immersion as estimated by gravimetric mass loss, H₂ collection, ICP-OES, and EIS-estimated R_p where $B_{King} = 36.0$ mV, $B_{Shi} = 36.8$ mV,⁵⁷ and $B_{CaO} = 31.1$ in 0.6 M NaCl were used.³⁹⁻⁴¹ The assumed uniform corrosion depth was determined from Equation (6). This depth must be amended as shown above.

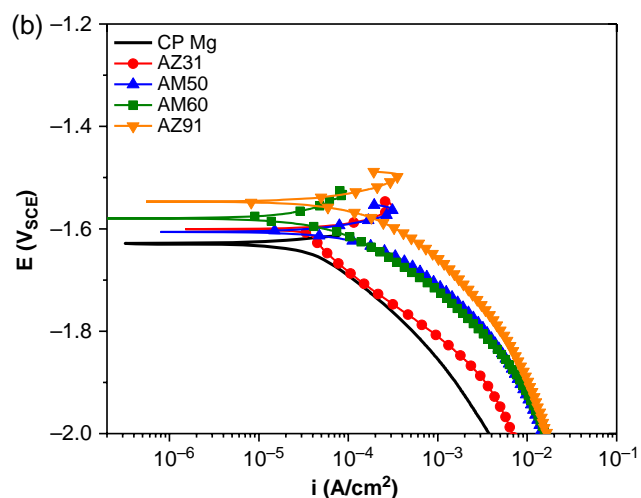
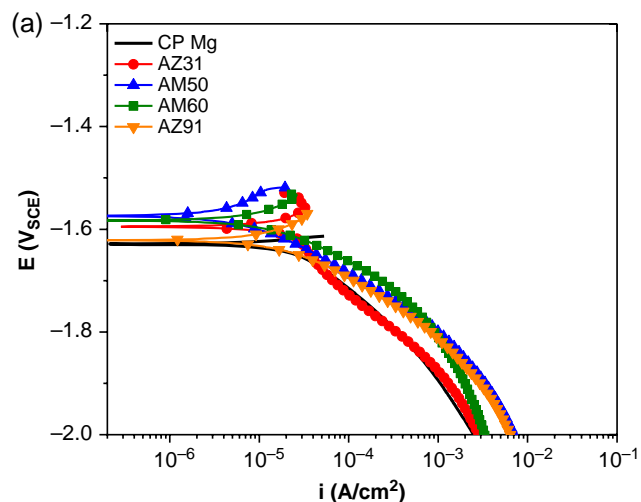


FIGURE 18. Typical cathodic polarization curves for 0.6 M NaCl after (a) 3 h at OCP and (b) 24 h at OCP.

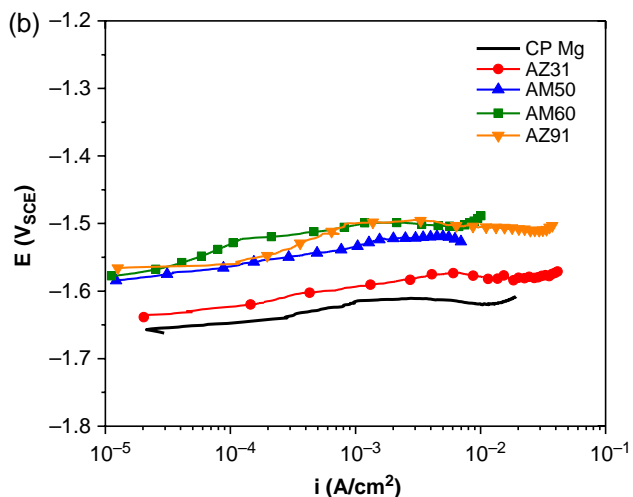
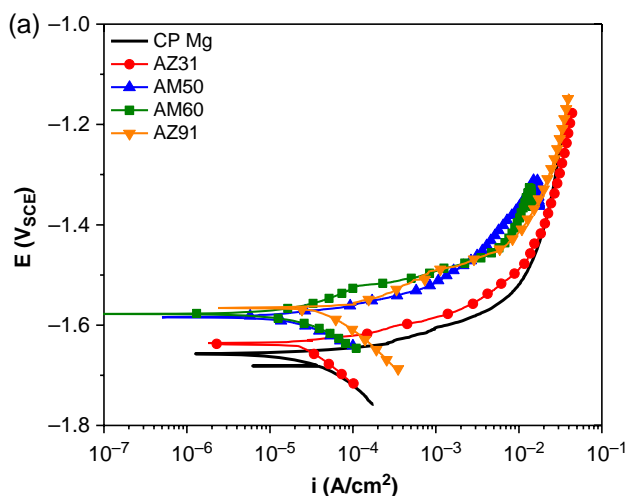


FIGURE 17. (a) Typical E - $\log(i)$ polarizations data for 0.6 M NaCl after 24 h at OCP and (b) IR-corrected net anodic E - $\log(i)$ plot.

intermetallics.²⁸⁻³⁰ However, between the three alloys, some trends in the initiation and propagation are seen. Corrosion typically initiated in the primary α -Mg matrix, which in some reports contains a lower Al content owing to solidification details and IMPs (Figures 10 through 12). It is unclear whether the corrosion was deeper with decreasing relative Al content resulting from low Al primary alpha grains, or simply more localized resulting from passivation brought about by high Al.

The β -phase ($Mg_{17}Al_{12}$) has several potential roles in corrosion and depends on morphology.¹⁹ This phase has been proposed to function as an active cathode (therefore increasing the microgalvanic coupling observed within the alloy between this phase and the α -matrix) and act as a "barrier" against lateral corrosion propagation from one primary α -Mg grain to another.^{7,19-20} In terms of microgalvanic corrosion between the primary α -Mg and the β -phase, as there is at least theoretically approximately the same amount of Al on average in solid solution for AM50, AM60, and

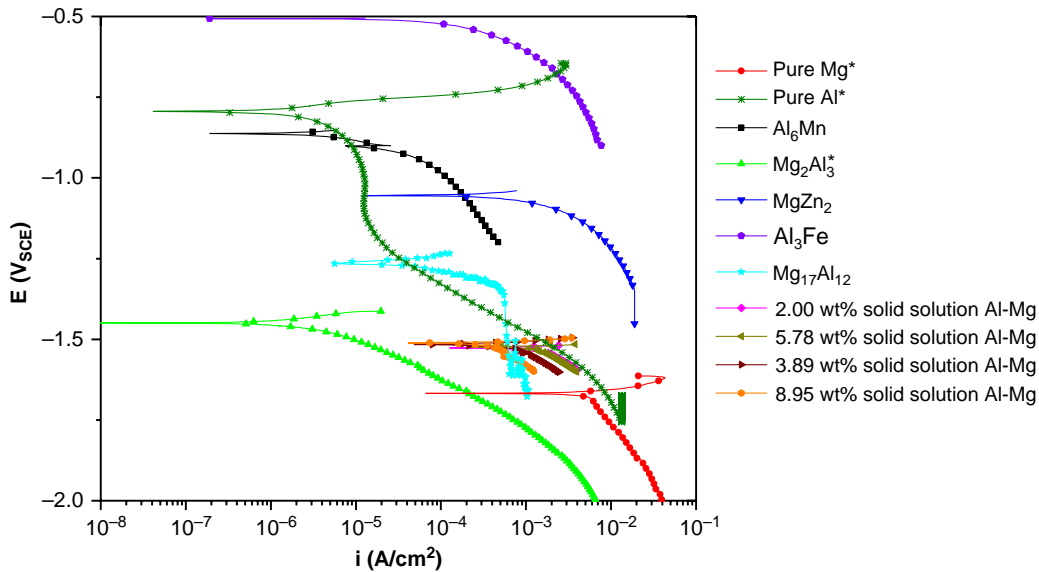


FIGURE 19. Various cathodic polarization curves taken for Al-containing IMPs in $[Cl^-]$ -containing environments. Curves replotted from the literature^{6,11,70,80} and augmented by the experimental data of this study (denoted by *). Information on the cathodic kinetics for these curves contained in Table 6.

AZ91, there would be approximately the same galvanic potential driving force between the α - and β -phases in each case. Moreover, it should be noted that the volume fraction of β -phase differs in these alloys, as seen in Table 2. Additionally, Figure 19 suggests that the precise chemical composition of the Al phase and the area fraction of Al-rich phases impacts the hydrogen

evolution reaction rate (HER) as a function of potential.^{6,69-70} In any case, it merits comment that the OCP of the primary α -Mg would likely be less noble than that of the Al-rich IMPs and solidification boundaries (formed during casting) and cause galvanic corrosion to occur as indicated by Table 7. Because of these differences in the electrochemical

TABLE 7
Literature Reported OCP and i_c for Various Al-Containing IMPs^{6,40,69,91} and Mg-Al Solid Solution Alloys^{70,92}

IMP	Solution	Immersion Time	pH	i_c (A/cm ²) Determined 100 mV Below E_{corr}	OCP (V _{SCE})	Ref
Al ₆ Mn	0.6 M NaCl	—	6	1×10^{-3}	-1.52	11,80
AlZn ₂	0.6 M NaCl	—	6	1×10^{-2}	-1.45	11,80
Mg ₁₇ Al ₁₂	0.1 M NaCl	—	6	1×10^{-5}	-1.2	6
Al ₃ Fe	0.6 M NaCl	—	6	1×10^{-2}	-0.74	11,80
Mg ₂ Al ₃	0.6 M NaCl	—	6	2×10^{-4}	-1.18	11,80
Mg-2 wt% Al ^(A)	0.85 M NaCl + Mg(OH) ₂	immediately after immersion	11	6×10^{-2}	-1.51	70
Mg-3.89 wt% Al ^(A)	0.85 M NaCl + Mg(OH) ₂	immediately after immersion	11	6×10^{-2}	-1.51	70
Mg-5.78 wt% Al ^(A)	0.85 M NaCl + Mg(OH) ₂	immediately after immersion	11	3×10^{-2}	-1.50	70
Mg-8.95 wt% Al ^(A)	0.85 M NaCl + Mg(OH) ₂	immediately after immersion	11	9×10^{-3}	-1.49	70
Mg-3.43 wt% Al ^(A)	ASTM D1384 water ^{93,(B)}	3 h	—	5×10^{-5}	-1.49	92
Mg-5.74 wt% Al ^(A)	ASTM D1384 water ⁹³	3 h	—	5×10^{-5}	-1.45	92
Mg-9.42 wt% Al ^(A)	ASTM D1384 water ⁹³	3 h	—	5×10^{-5}	-1.40	92
Mg-5.74 wt% Al-1.19 wt% Zn ^(A)	ASTM D1384 water ⁹³	3 h	—	1×10^{-4}	-1.43	92
Mg ₁₇ Al ₁₂	ASTM D1384 water ⁹³	3 h	—	1×10^{-3}	-1.31	92
Mg ₁₇ (Al, Zn) ₁₂	ASTM D1384 water ⁹³	3 h	—	5×10^{-4}	-1.24	92
Mg-6Zn ³	ASTM G31 ⁹⁴	—	—	5×10^{-4}	-1.56	95
Mg ₁₇ (Al, Zn) ₁₂	0.1 M NaClO ₄	—	—	1×10^{-3}	-1.71	96
Al-5.5 Mn	0.138 M MgCl ₂	12 h	6	5×10^{-6}	-0.85	88
Al-5.5 Mn	0.275 M NaCl	12 h	6	5×10^{-6}	-0.75	88
Al-13.5 Mn	0.138 M MgCl ₂	12 h	6	3×10^{-6}	-0.95	88
Al-13.5 Mn	0.275 M NaCl	12 h	6	3×10^{-6}	-0.95	88

^(A) Single phase alloy.

^(B) The specified corrosive water can be prepared by dissolving 148 mg sodium sulfate, 165 mg sodium chloride, and 139 mg sodium bicarbonate in 1 L of distilled or deionized water.

potential between the primary α -Mg and the solidification boundaries, as well as IMPs, microgalvanic coupling between these phases would lead to the corrosion damage morphologies seen in Mg alloys especially if corrosion initiates and propagates in Al lean α -Mg grains (Figures 10 through 12, Table 7). However, the β -phase is not nearly as strong of a cathode as other IMPs such as Al_3Fe or Al_6Mn , as indicated by Figure 19.

Corrosion typically initiated in the primary α -Mg in close proximity to the β -phase as well as near Al-Mn-Fe containing IMPs for AM50, AM60, and AZ91 (Figures 7 through 9) where these secondary phases functioned as active cathodes. However, the global corrosion rate in these high Al-content alloys is much lower than seen previously for AZ31⁵⁹ (Figure 16). During propagation, the corrosion remained in specific, isolated primary α -Mg grains (which is typically surrounded by β -phase and/or eutectic $\alpha+\beta$) and did not propagate beyond into the surrounding β -phase and/or eutectic $\alpha+\beta$. This is shown in Figure 12(c) in particular. Therefore, the β -phase provides a galvanic driving force for corrosion initiation in the primary α -Mg phase, but also limits propagation in the alloy because of the lateral barrier to filiform type attack morphology and notable modest HER rates on β -phase (Figure 19).

The degree of localized corrosion (at the primary α -Mg/ β -phase interface) versus uniform corrosion was compared for CP Mg, AZ31, AM50, AM60, and AZ91 using the LF (Equation [7]). The LF is the ratio of the maximum penetration depth to the average depth (Equation [6]). Therefore, the higher the LF, the higher the degree of localized corrosion damage. From this assessment, CP Mg has a lower LF than any of the die-cast alloys, while AM60 and AZ91 have the highest LF (Table 8). Therefore, while AM60 and AZ91 have lower overall (assumed uniform) corrosion rates, they experience extensive localized corrosion, such as the localized microgalvanic corrosion between the primary α -Mg matrix and IMPs. Normalization of the low corrosion rates stated, taking into account the LF, suggesting a much higher localized corrosion rate. Speculatively, primary α -Mg with a basal orientation

and/or of low Al content is preferentially attacked next to the $\alpha+\beta$ eutectic or β -phase, which can cause the seemingly random incidence of corrosion at this interface. However, this issue cannot be addressed further with the data available from this study and could be proposed as a future avenue for research.

Comparison of Corrosion Rate of AM50, AM60, and AZ91

To date, it has been generally accepted that the addition of Al within Mg alloys increases the corrosion resistance when alloying remains in solid solution.^{24,71-73} However, there is some debate on whether or not the addition of Al above 4 wt% will increase the corrosion rate.⁴⁶ Some studies have shown that Al additions up to 5 wt% to 9 wt% increase the corrosion resistance.⁷⁴⁻⁷⁶ However, other studies shown that high Al-content alloys, such as AZ91 have a decreased corrosion resistance.⁷⁷ One potential source of this discrepancy in corrosion rate is brought about by the fact that, during dissolution, the near-surface pH can rise to alkaline levels (pH >10) for Mg, and the surface of Mg also displays enhanced catalytic HER activity (i.e., ability to support the cathodic HER reaction) as shown by independent works.⁴³⁻⁷⁸ Al surface enrichment and incorporation in oxides could lower rates.^{10-11,30,79} The time dependency and interplay between these various phenomena could change trends in short-term test versus long-term test results as the surface, electrolyte, and relative rates of reaction become altered with time. In a direct comparison of the die-cast alloys, using four parallel techniques, it is shown that an increase in the Al content increases the global corrosion resistance for die-cast alloys (Figure 16, Tables 5 and 6), confirmed or independently corroborated for the four methods used here. The four, parallel methods, were able to yield repeatable values of the corrosion rate, showing that, for full immersion tests, at OCP in chloride-containing environments the accumulated charge per unit area decreases with increasing Al content. The methodology also demonstrates the validity of the EIS method for these alloys as well as the fact that the corrosion mechanisms in α -Mg remains relatively similar following a charge transfer controlled Mg^{2+} overall process and is altered by Al with an adsorbed intermediate that responds to potential.

This variation in the corrosion rate with alloying content has to be considered in terms of the amount of Al in solid solution versus the Al partitioned to IMPs. For AM50, AM60, and AZ91, the Al in solid solution on average (neglecting non-equilibrium solidification effects) is approximately the same (~2 wt%). However, there is also a variation in the volume fraction of second phases and the composition of these secondary phases specific to each alloy (Table 2). In particular, the β -phase is not present in AZ31B but is present in

TABLE 8

Localization Factor for CP Mg and Mg-Al Alloys as Determined Through Equations (6) and (7) After Exposure in 0.6 M NaCl for 24 Hours

	Assumed Uniform Penetration Depth (μm)	Maximum Penetration Depth (μm)	Localization Factor (LF)
Mg Rod	70	300	4.3
AZ31B-H24	22	100	4.5
AM50A	10	100	10
AM60B	8	200	25
AZ91D	5	300	60

AM50, AM60, and AZ91 (Table 2), along with a higher phase fraction of Al_2Mn_3 , Al_3Fe , and $\text{Al}_8\text{Mn}_5(\text{Fe})$. More specifically, the β -phase and eutectic $\alpha+\beta$ appears in AM50, AM60, and AZ91. From recent literature, the cathodic reaction rates of these IMPs are of the order of 10^{-3} A/cm² to as low as 10^{-5} A/cm², while the OCP is anywhere from -1.6 V_{SCE} to -0.5 V_{SCE} depending on composition^{6,10-11,80} (Table 7). It is noted that, examining the cathodic polarization curves of solid solution alloys with increasing amounts of Al,⁷⁰ the cathodic reaction rates generally decrease with increasing Al content, especially when Fe is not present (Figure 19),⁷⁰ despite the strong positive trends in the OCPs. This suggests that the action of Al content on the anodic reaction rate affects the OCP more than its influence on the cathodic reaction rate. Therefore, both the effect of Al in solid solution on the anodic kinetics of Mg dissolution in the primary α -Mg solid solution and the effect of Al-rich IMP cathodes are both factors in determining the corrosion rate of Mg-Al alloys.

Variation in Kinetics on Mg-Al Alloys with Al Content

From examining the IR corrected data, there is a decrease in the anodic reaction rate with increasing Al content (Figure 17[a]) which agrees with literature.⁴⁶ An additional benefit is the random texture in die-cast alloys versus wrought alloys with predominantly basal texture.⁸¹ There is also surprisingly little difference in the cathodic kinetics (in the initial 3 h) when Al is alloyed with Mg (Figure 18[a]), particularly as limited corrosion initiation was observed in the first 3 h to 4 h. However, cathodic HER kinetics are enhanced after ~24 h, as shown in Figure 18(b). There was no variation in the cathodic kinetics for all times and alloys in 0.6 M NaCl buffered with TRIS to pH ~7 as well as 0.1 M TRIS, possibly resulting from buffering, restriction in hydroxide film formation, and inability to incorporate Al in hydroxides.

Variations in the cathodic kinetics with time, environment, and alloying content are likely a result of the variation in the oxide identity based on the environment and elements. It has been shown previously that the precipitation of $\text{Mg}(\text{OH})_2$ in chloride environments can strongly affect the corrosion morphology, corrosion rate, and cathodic activation.^{10-11,45,59,81} Therefore, the overall more rapid corrosion rates on CP Mg and AZ31 will lead to higher dissolution and consequently a thicker hydroxyl film during corrosion in unbuffered NaCl. This film will locally render the sample surface more alkaline and may lead to larger changes in the cathodic kinetics with time. This is particularly observed in Figures 18(a) and (b) where the cathodic kinetics after 3 h do not vary with increasing Al alloyed content but after 24 h the cathodic kinetics increase to a greater extent with increasing Al content.

Variation in Al Composition and Effect of Al Redeposition on the Anodically-Induced Cathodic Activation of Mg Alloys

A recently cited phenomenon in Mg corrosion is the anodically-induced cathodic activation.^{78,82-85} The corrosion rate of the Mg increases over time because of changes in the cathodic kinetics at the sample surface.⁸⁴⁻⁸⁵ Cathodic activation can first be considered as a function of exposure environment. The starting pH of 0.6 M NaCl was measured to be approximately 5.3 with the pH changing to approximately 11. This increased alkalinity of the exposure environment, particularly at the sample surface, could lead to the dissolution of Al on the sample surface as well as the redeposition of Al as $\text{Al}(\text{OH})_3$ away from the IMP interface²⁹⁻³⁰ where the pH may differ. A potential explanation for the variation in cathodic kinetics with time is enrichment of both Al and/or transition elements to the sample surface⁸⁶⁻⁸⁷ as well as AlO_2^- dissolution as a consequence of the alkalization of the sample surface to pH > 11.^{30,82,87-88} The strong effect of pH on cathodic activation is confirmed via tests in 0.1 M TRIS and 0.6 M NaCl buffered with TRIS environments where cathodic activation does not occur.^{10-11,45} Both of these environments start with a pH of ~7 and, even after a 24 h immersion, maintain a pH of ~7. At this near-neutral pH, the dissolution and redeposition of alloying elements onto the sample surface is not thermodynamically possible³⁸ and, therefore, less cathodic activation occurs. This was observed in 0.1 M TRIS which shows little to no cathodic activation.^{10-11,45}

Cathodic activation can also be considered as a function of alloy composition. Examining the composition of the alloys in this study (Table 1), it is shown that the CP Mg rod contained the highest Fe content, which has been previously detected to enrich to the metal/oxide interface.⁸² This may lead to differences in the cathodic activation process over time as a result of enrichment of this transition element to the sample surface.⁸⁷ Considering variation in the cathodic kinetics and OCP with time for the die-cast alloys, as well as the previously studied commercially pure Mg and AZ31 in 0.6 M NaCl,^{10-11,45,59} an assessment can be made on the amount of cathodic activation seen for each of these systems and how it relates to the alloying content. The greatest amount of cathodic activation (the largest variation in the cathodic kinetics and OCP) was observed for the CP Mg material as well as AZ31B-H24 (Figures 13 and 18). There was a slight increase in the cathodic kinetics and OCP for AM50 and AM60 over the 24 h in 0.6 M NaCl, and a negligible amount of cathodic activation for AZ91 over the 24 h; this was much less than determined previously for lower Al-content alloys (Figures 13 and 18). The variation in the cathodic kinetics and OCP can also be rationalized through considering the variation in $\text{Mg}(\text{OH})_2$ formation. The CP Mg and AZ31 samples have the highest overall corrosion rates and therefore will produce

more $\text{Mg}(\text{OH})_2$ which may retain dissolved alloying elements and trap transition metal elements which can increase the cathodic kinetics and OCP more rapidly with time.^{30,88} From the EIS-determined anodic charge produced in 0.6 M NaCl (Figure 16), the intrinsic corrosion rate for AM50A, AM60B, and AZ91D were much lower than AZ31B and CP Mg. The lower corrosion rate may lead to less dissolution of the Mg and Al and therefore less enrichment of alloying elements to the sample surface.^{82,87,89-90}

CONCLUSIONS

❖ An accurate and repeatable method to determine the intrinsic corrosion rate of a variety of die-cast Mg-Al alloys has been used herein. Each of the four methods provided (EIS analysis, mass loss, H_2 gas collection, and ICP-OES solution analysis) gives a straightforward approach and enables calculation of the corrosion rate by corroborating methods under OCP conditions which has been shown herein to be useful for high (≥ 3 wt%) Mg-Al alloys.

❖ In order to accurately determine the corrosion rate for Mg alloys in chloride-containing environments, various plausible Tafel slope assumptions are tolerable in the Stern-Geary approach. The EIS-determined R_p dominates the Stern-Geary expression utilized for corrosion rate determination. However, appropriate use of the low-frequency inductive loop must be considered as this inductive loop is often seen in many Mg alloys in unbuffered 0.6 M NaCl, as reported to date, in chloride-containing environments. This implies that the corrosion rate even when effected by microgalvanic couples is similar for a number of Mg-Al and Mg-Al-Zn alloys in NaCl. The careful consideration of the full inductive time constant gives a repeatable measurement of the EIS-determined corrosion rate. It is proposed herein that Mg dissolves as Mg^{2+} overall with a strong role of adsorbed intermediates. This anodic half-cell reaction controls OCP corrosion.

❖ The corrosion rates for commercially pure Mg, AZ31, AM50, AM60, and AZ91 have been compared, and it is seen that the corrosion rate decreases globally with increasing Al content. However, the localization factor increases with Al content; therefore, normalization of the overall corrosion across the surface versus at specific active sites must be understood. Deeper "local" corrosion occurs in the die-cast alloys with ≥ 3 wt% Al content.

❖ In terms of microstructure, the corrosion initiates in selected α -Mg, frequently proximate to the Al-rich β -phase or Al-Mn IMPs in the die-cast alloys with ≥ 3 wt% Al content.

❖ The corrosion behavior of the β -phase is complex. This IMP may function as a cathode during microgalvanic corrosion of the α - and β -phases, as seen in the initiation of the corrosion process; it can also act as a lateral barrier to the propagation of corrosion damage from one damage site, as seen in how the corrosion

propagation remains localized to single α -Mg grains. The variation in this behavior has to do with the variation in the initiation and propagation behavior of the corrosion within the Mg-Al alloys.

❖ Variations in the cathodic kinetics and amounts of cathodic activation were observed with exposure environment as well as alloying content. Higher amounts of cathodic activation were observed in the alkaline environments, potentially resulting from the corrosion and redeposition of alloying elements (such as Al) onto the sample surface. There was less cathodic activation in the higher Al content alloys, both because of the lower corrosion rates of the die-cast alloys and modest HER reactions on the β -phase.

ACKNOWLEDGMENTS

This student (LB) was funded by the Office of Naval Research Grant N000141210967 with Dr. David A. Shifler as scientific officer. The NSF under DMR-130999 and ONR under Grant SP0028970-PROJ0007990 supported JRS. The U.S. Government is authorized to reproduce and distribute reprints for Governmental purposes notwithstanding any copyright notation thereon. The views and conclusions contained herein are those of the authors and should not be interpreted as necessarily representing the Office of Naval Research and the Technical Corrosion Collaboration. The help of Prof. Nick Birbilis especially with regard to technical advice during his visit to UVA, as well as to providing cathodic polarization data shown in Figure 19 is gratefully acknowledged.

REFERENCES

1. M. Esmaily, M. Shahabi-Navid, J.E. Svensson, M. Halvarsson, L. Nyborg, Y. Cao, L.G. Johansson, *Corros. Sci.* 90 (2015): p. 420-433.
2. M.M. Avedesian, H. Baker, *Magnesium and Magnesium Alloys* (Materials Park, OH: ASM International, 1999).
3. A.A. Luo, *J. Magn. Alloys* 1, 1 (2013): p. 2-22.
4. R.E. Reed-Hill, R. Abbaschian, *Physical Metallurgy Principles* (Boston, MA: PWS-Kent Pub., 1992).
5. R.M. Wang, A. Eliezer, E. Gutman, *Mater. Sci. Eng. A* 344, 1-2 (2003): p. 279-287.
6. A.D. Südholz, N.T. Kirkland, R.G. Buchheit, N. Birbilis, *Electrochem. Solid-State Lett.* 14, 2 (2011): p. C5-C7.
7. O. Lunder, J.E. Lein, T.K. Aune, K. Nisancioglu, *Corrosion* 45, 9 (1989): p. 741-748.
8. O. Lunder, T.K. Aune, K. Nisancioglu, *Corrosion* 43, 5 (1987): p. 291-295.
9. Y. Wang, M. Xia, Z. Fan, X. Zhou, G.E. Thompson, *Intermetallics* 18 (2010): p. 1683-1689.
10. L.G. Bland, J.J. Bhattacharyya, S.R. Agnew, J.R. Scully, *ECS Meet. Abstracts MA2016-02* (2016): p. 1327.
11. L.G. Bland, N. Birbilis, J.R. Scully, *J. Electrochem. Soc.* 163, 14 (2016): p. C895-C906.
12. V.Y. Gertsman, J. Li, S. Xu, J.P. Thomson, M. Sahoo, *Metall. Mater. Trans. A* 36, 8 (2005): p. 1989-1997.
13. S. Feliu Jr., A. Pardo Feliu, M.C. Merino, A.E. Coy, F. Viejo, R. Arrabal, *Appl. Surf. Sci.* 255, 7 (2009): p. 4102-4108.
14. S. Feliu Jr., C. Maffiotte, A. Samaniego, J.C. Galvan, V. Barranco, *Appl. Surf. Sci.* 257, 20 (2011): p. 8558-8568.
15. M. Jönsson, D. Persson, R. Gubner, *J. Electrochem. Soc.* 154, 11 (2007): p. C684-C691.
16. M. Jönsson, D. Persson, C. Leygraf, *Corros. Sci.* 50, 5 (2008): p. 1406-1413.

17. R.K. Singh Raman, N. Birbilis, J. Efthimiadis, *Corros. Eng. Sci. Technol.* 39, 4 (2004): p. 346-350.
18. G. Song, A. Atrens, X. Wu, B. Zhang, *Corros. Sci.* 40, 10 (1998): p. 1769-1791.
19. M.C. Zhao, M. Liu, G. Song, A. Atrens, *Corros. Sci.* 50, 7 (2008): p. 1939-1953.
20. G. Song, *Adv. Eng. Mater.* 7, 7 (2005): p. 563-586.
21. B.-L. Yu, J.-Y. Uan, *Metall. Mater. Trans. A* 36, 8 (2005): p. 2245-2252.
22. R.K. Singh Raman, *Metall. Mater. Trans. A* 35, 8 (2004): p. 2525-2531.
23. T. Beldjoudi, C. Fiaud, L. Robbiola, *Corrosion* 49, 9 (1993): p. 738-745.
24. G.L. Makar, J. Kruger, *J. Electrochem. Soc.* 137, 2 (1990): p. 414-421.
25. S. Mathieu, C. Rapin, J. Hazan, P. Steinmetz, *Corros. Sci.* 44, 12 (2002): p. 2737-2756.
26. A. Pardo, M.C. Merino, A.E. Coy, F. Viejo, R. Arrabal, S. Feliu Jr., *Electrochim. Acta* 53, 27 (2008): p. 7890-7902.
27. I.J. Polmear, *Light Alloys: Metallurgy of the Light Metals*, 3rd ed. (Oxford, United Kingdom: Butterworth-Heinemann, 1995), p. 362.
28. R.M. Asmussen, P. Jakupi, M. Danaie, G.A. Botton, D.W. Shoesmith, *Corros. Sci.* 75 (2013): p. 114-122.
29. M. Danaie, R.M. Asmussen, P. Jakupi, D.W. Shoesmith, G.A. Botton, *Corros. Sci.* 77 (2013): p. 151-163.
30. M. Danaie, R.M. Asmussen, P. Jakupi, D.W. Shoesmith, G.A. Botton, *Corros. Sci.* 83 (2014): p. 299-309.
31. N. LeBozec, M. Jönsson, D. Thierry, *Corrosion* 60, 4 (2004): p. 356-361.
32. J. Liao, M. Hotta, S.-I. Motoda, T. Shinohara, *Corros. Sci.* 71 (2013): p. 53-61.
33. C.A. Walton, H.J. Martin, M.F. Horstemeyer, P.T. Wang, *Corros. Sci.* 56 (2012): p. 194-208.
34. D.A. Jones, *Principles and Prevention of Corrosion*, 2nd ed. (Upper Saddle River, NJ: Prentice Hall, 1995).
35. T. Cain, L.G. Bland, N. Birbilis, J.R. Scully, *Corrosion* 70, 10 (2014): p. 1043-1051.
36. G. Song, A. Atrens, *Adv. Eng. Mater.* 1, 1 (1999): p. 11-33.
37. J.H. Nordlien, S. Ono, N. Masuko, K. Nisancioglu, *J. Electrochem. Soc.* 142, 10 (1995): p. 3320-3322.
38. M. Pourbaix, *Atlas of Electrochemical Equilibria in Aqueous Solutions* (Houston, TX: NACE International, 1974).
39. A.D. King, N. Birbilis, J.R. Scully, *Electrochim. Acta* 121, 1 (2014): p. 394-406.
40. L.G. Bland, A.D. King, N. Birbilis, J.R. Scully, *Corrosion* 71, 2 (2015): p. 128-145.
41. I.B. Singh, M. Singh, S. Das, *J. Magn. Alloys* 3, 2 (2015): p. 142-148.
42. J.R. Scully, *Corrosion* 56 (2000): p. 199-218.
43. J. Świątowska, P. Volovitch, K. Ogle, *Corros. Sci.* 52 (2010): p. 2372-2378.
44. S. Lebouil, A. Duboin, F. Monti, P. Tabeling, P. Volovitch, K. Ogle, *Electrochim. Acta* 124 (2014): p. 176-182.
45. L.G. Bland, B.C. Rincon Troconis, R.J. Santucci Jr., J.M. Fitz-Gerald, J.R. Scully, *Corrosion* 72, 10 (2016): p. 1226-1242.
46. K. Gusieva, C.H.J. Davies, J.R. Scully, N. Birbilis, *Int. Mater. Rev.* 60 (2015): p. 169-194.
47. "AZtecEnergy: EDS Software," Oxford Instruments 2015.
48. ASTM E112, "Standard Test Methods for Determining Average Grain Size" (West Conshohocken, PA: ASTM International, 2013).
49. ASTM G1, "Standard Practice for Preparing, Cleaning, and Evaluating Corrosion Test Specimens" (West Conshohocken, PA: ASTM International, 2011).
50. C.A. Schneider, W.S. Rasband, K.W. Eliceiri, *Nat. Methods* 9 (2012): p. 671-675.
51. M. Curioni, F. Scenini, T. Monetta, F. Bellucci, *Electrochim. Acta* 166 (2015): p. 372-384.
52. G. Baril, N. Pebere, *Corros. Sci.* 43, 3 (2001): p. 471-484.
53. G. Baril, G. Galicia, C. Deslouis, N. Pebere, B. Tribollet, V. Vivier, *J. Electrochem. Soc.* 154, 2 (2007): p. C108-C113.
54. J.L. Bullister, N.L. Guinasso Jr., D.R. Schink, *J. Geophys. Res. Oceans* 87, C3 (1982): p. 2022-2034.
55. M. Stern, A.L. Geary, *J. Electrochem. Soc.* 104, 1 (1957): p. 56-63.
56. F.Y. Cao, Z.M. Shi, J. Hofstetter, P.J. Uggowitzer, G.L. Song, M. Liu, A. Atrens, *Corros. Sci.* 75 (2013): p. 78-99.
57. Z. Shi, F. Cao, G.L. Song, M. Liu, A. Atrens, *Corros. Sci.* 76 (2013): p. 98-118.
58. ASTM G106, "Standard Practice for Verification of Algorithm and Equipment for Electrochemical Impedance Measurements" (West Conshohocken, PA: ASTM International, 2010).
59. L.G. Bland, J.M. Fitz-Gerald, J.R. Scully, *Corrosion* 72, 9 (2016): p. 1116-1132.
60. G. Song, A. Atrens, D. St John, X. Wu, J. Nairn, *Corros. Sci.* 39, 10-11 (1997): p. 1981-2004.
61. G. Baril, C. Blanc, M. Keddam, N. Pebere, *J. Electrochem. Soc.* 150, 10 (2003): p. B488-B493.
62. G. Baril, C. Blanc, N. Pebere, *J. Electrochem. Soc.* 148, 12 (2001): p. B489-B496.
63. I. Nakatsugawa, R. Martin, E.J. Knystautas, *Corrosion* 52, 12 (1996): p. 921-926.
64. Y.C. Xin, C.L. Liu, W.J. Zhang, J. Jiang, G. Tang, X.B. Tian, P.K. Chu, *J. Electrochem. Soc.* 155, 5 (2008): p. C178-C182.
65. A.M. Fekry, M.A. Ameer, *Int. J. Electrochem. Sci.* 6, 5 (2011): p. 1342-1354.
66. B. Hirschorn, M.E. Orazem, B. Tribollet, V. Vivier, I. Frateur, M. Musiani, *J. Electrochem. Soc.* 157, 12 (2010): p. C458-C463.
67. B. Hirschorn, M.E. Orazem, B. Tribollet, V. Vivier, I. Frateur, M. Musiani, *J. Electrochem. Soc.* 157, 12 (2010): p. C452-C457.
68. B. Hirschorn, M.E. Orazem, B. Tribollet, V. Vivier, I. Frateur, M. Musiani, *Electrochim. Acta* 55, 21 (2010): p. 6218-6227.
69. G. Song, A. Atrens, *Adv. Eng. Mater.* 5, 12 (2003): p. 837-858.
70. G. Song, A.L. Bowles, D.H. St John, *Mater. Sci. Eng. A* 366, 1 (2004): p. 74-86.
71. E. Ghali, W. Dietzel, K.U. Kainer, *J. Mater. Eng. Perform.* 13, 1 (2004): p. 7-23.
72. I.J. Polmear, *Light Alloys: From Traditional Alloys to Nanocrystals*, 4th ed. (Amsterdam, The Netherlands: Elsevier, 2006).
73. P. Hoyer, G.L. Angrisani, C. Klose, F.W. Bach, T. Hassel, *Mater. Corros.* 65, 1 (2014): p. 23-30.
74. O. Lunder, J.E. Lein, T.K. Aune, K. Nisancioglu, *Corrosion* 45 (1989): p. 741-748.
75. F.H. Froes, Y.-U. Kim, F. Hehman, *J. Metals* 39 (1987): p. 14-21.
76. O. Lunder, J.H. Nordien, K. Nisancioglu, *Corros. Rev.* 15, 3-4 (1997): p. 439-469.
77. Y.L. Cheng, T.W. Qin, H.M. Wang, Z. Zhang, *Trans. Nonferr. Metal Soc. China* 19 (2005): p. 517-524.
78. G. Williams, N. Birbilis, H.N. McMurray, *Electrochem. Comm.* 36 (2013): p. 1-5.
79. L.G. Bland, R.F. Schaller, J.R. Scully, "Utilization of a Partially Non-Aqueous Electrolyte for the Spatial Mapping of Mg Corrosion Using a Model Mg-Al Electrode," 2017 TMS Annual Meeting & Exhibition (Warrendale, PA: The Minerals, Metals and Materials Society, 2017).
80. N. Birbilis, R.G. Buchheit, *J. Electrochem. Soc.* 152, 4 (2005): p. B140-B151.
81. L.G. Bland, K. Gusieva, J.R. Scully, *Electrochim. Acta* 227 (2017): p. 136-151.
82. M. Taheri, J.R. Kish, N. Birbilis, M. Danaie, E.A. McNally, J.R. McDermid, *Electrochim. Acta* 116 (2014): p. 396-403.
83. N. Birbilis, A.D. King, S. Thomas, G.S. Frankel, J.R. Scully, *Electrochim. Acta* 132 (2014): p. 277-283.
84. G.S. Frankel, S. Fajardo, B.M. Lynch, *Faraday Discussions* 180 (2015): p. 11-33.
85. G.S. Frankel, A. Samaniego, N. Birbilis, *Corros. Sci.* 70 (2013): p. 104-111.
86. S. Fajardo, G.S. Frankel, *Electrochim. Acta* 165 (2015): p. 255-267.
87. T. Cain, S.B. Madden, N. Birbilis, J.R. Scully, *J. Electrochem. Soc.* 162, 6 (2015): p. C228-C237.
88. R.M. Asmussen, W.J. Binns, R. Partovi-Nia, P. Jakupi, D.W. Shoesmith, *Mater. Corros.* 67, 1 (2016): p. 39-50.
89. Z.P. Cano, M. Danaie, J.R. Kish, J.R. McDermid, G.A. Botton, G. Williams, *Corrosion* 71, 2 (2015): p. 146-159.
90. Z.P. Cano, J.R. McDermid, J.R. Kish, *J. Electrochem. Soc.* 162, 14 (2015): p. C732-C740.
91. E. Ghali, "Magnesium and Magnesium Alloy," in *Uhlig's Corrosion Handbook*, 2nd ed. (New York, NY: John Wiley & Sons, 2000), p. 793-830.
92. S. Mathieu, C. Rapin, J. Steinmetz, P. Steinmetz, *Corros. Sci.* 45, 12 (2003): p. 2741-2755.
93. ASTM D1384, "Standard Test Method for Corrosion Test for Engine Coolants in Glassware" (West Conshohocken, PA: ASTM International, 2012).
94. ASTM G31, "Standard Guide to Laboratory Immersion Corrosion Testing of Materials" (West Conshohocken, PA: ASTM International, 2015).
95. S. Zhang, X. Zhang, C. Zhao, J. Li, Y. Song, C. Xie, H. Tao, Y. Zhang, Y. He, Y. Jiang, Y. Bian, *Acta Biomater.* 6, 2 (2010): p. 626-640.
96. H. Krawiec, S. Stanek, V. Vignal, J. Lelito, J.S. Suchy, *Corros. Sci.* 53, 10 (2011): p. 3108-3113.